

# ~~A Code-to-Code Comparison for Floating Offshore Wind Turbine Simulation in Realistic Environmental Conditions: Quantifying the Impact of Modeling Fidelity on Different Substructure Concepts - Part II: Code-to-Code Comparison in Realistic Environmental Conditions~~

Francesco Papi<sup>1</sup>, Giancarlo Troise<sup>2</sup>, Robert Behrens de Luna<sup>3</sup>, Joseph Saverin<sup>3</sup>, Sebastian Perez-Becker<sup>3</sup>, David Marten<sup>3</sup>, Maire-Laure Ducasse<sup>4</sup>, Alessandro Bianchini<sup>1</sup>

<sup>1</sup>Department of Industrial Engineering, University of Florence, Firenze, 50139, Italy

<sup>2</sup>Seapower srl, Naples, 80121, Italy

<sup>3</sup>Hermann Föttinger Institute, Technical University of Berlin, Berlin, 10623, Germany

<sup>4</sup>Saipem S.A., 1/7 Avenue San Fernando, 78884 Saint Quentin Yvelines cedex, France

Correspondence to: A. Bianchini ([alessandro.bianchini@unifi.it](mailto:alessandro.bianchini@unifi.it)) or F. Papi ([fr.papi@unifi.it](mailto:fr.papi@unifi.it))

**Abstract.** Consensus is arising on considering floating offshore wind as the most promising ~~technologies~~ technology to increase renewable energy generation offshore. While evolving ~~fast~~ quickly from a technological point of view, Floating Offshore Wind Turbines (FOWTs) are challenging, as their performance and loads are governed by complex dynamics that are a result of the coupled influence of wind, waves, and currents on the structures. Many open challenges ~~are~~ therefore still ~~in place~~ exist, especially from a modeling perspective. This study contributes to the understanding of the impact of modeling differences on FOWT loads by comparing three FOWT simulation codes, QBlade-Ocean, OpenFAST, and DeepLines Wind<sup>®</sup> and three substructure designs, a semi-submersible, a spar-buoy, and the two-part concept Hexafloat in realistic environmental conditions. This extensive comparison represents one of the main outcomes of the H2020 project FLOATECH. In accordance with international standards for FOWT certification, multiple design situations are compared, including operation in normal power production and parked conditions. Results show that the compared codes agree well in the prediction of the system dynamics, regardless of the fidelity of the underlying modeling theories. Some differences between the codes emerged however in the analysis of fatigue loads, where, contrary to extreme loads, specific trends can be noted. With respect to QBlade-Ocean, OpenFAST was found to overestimate lifetime damage equivalent loads up to 14%. DeepLines Wind<sup>®</sup>, on the other hand, underestimated lifetime fatigue loads by up to 13.5%. Regardless of the model and FOWT design however, differences in fatigue loads are larger for tower base loads than for blade root loads, due to the larger influence substructure dynamics have on these loads.

## 1 Introduction

In recent years industrial and academic interest around floating offshore wind energy has been increasing, thanks to its promise to foster wind energy harvesting in offshore areas previously inaccessible with bottom-fixed wind turbines. To fully exploit the

32 advantages of this technology, ever larger and more flexible offshore turbines are being developed and deployed. These systems  
33 are challenging to model, as their dynamics are governed by the coupled influence of aerodynamics, hydrodynamics, control,  
34 and moorings. As an additional complexity, with large and flexible turbine rotors, aeroelastic coupling also plays an important  
35 role. Many of the industry’s work-horse simulation codes have been developed with smaller, more rigid, bottom-fixed rotors in  
36 mind and rely on engineering models, sometimes empirically derived, to model the relevant physical phenomena. In this context,  
37 a real need for verification and validation of these tools exists. Several efforts, past and present, have been put into verification  
38 and validation of offshore simulation codes. Notable examples being the Offshore Code Comparison (“OC” in short) programs  
39 promoted by the International Energy Agency (IEA), OC3, OC4, OC5 and the on-going OC6 (Jonkman and Musial, 2010;  
40 Robertson et al., 2014b, 2017; Bergua and et. al., 2023). Throughout the OC- projects, offshore codes have been compared  
41 against other codes, and against wave-tank experiments. Especially OC4 and OC5 have helped highlight deficiencies in low-  
42 frequency hydrodynamic modeling of semi-submersible type platforms (Robertson et al., 2017) that have allowed the advance  
43 of the state-of-the art in OC6 (Robertson et al., 2020; Wang et al., 2022). Most of these campaigns have found that even simplified  
44 engineering tools are generally able to capture the aerodynamics of these systems well - at times better than expected, such as in  
45 (Bergua and et. al., 2023) – when compared to higher-fidelity and more physically complete aerodynamic models. Throughout  
46 these comparison studies however, a limited number of often simplified inflow conditions have been tested. On the other hand,  
47 some authors have found some differences between modeling theories when the coupled system dynamics are put to the test. In  
48 particular, ~~Corniglion~~ (Corniglion, (2022) found increased blade root fatigue loads when comparing Blade Element Momentum  
49 Theory (BEMT) to a higher fidelity Lifting-Line Free Vortex Wake (LLFVW) method. Similar considerations were also drawn  
50 by other authors such as (Boorsma et al., 2020; Perez-Becker et al., 2020) when comparing fatigue load predictions on onshore  
51 wind turbines. In detail, Boorsma et al. (Boorsma et al., 2020) have linked the increase in fatigue loads to increased 1P load  
52 variation, while Perez-Becker et al. (Perez-Becker et al., 2020) have found that even small differences in aerodynamic modeling  
53 can lead to different controller reactions, influencing overall loading and highlighting the importance of accurately modeling the  
54 entire coupled dynamics of the system. In the case of FOWTs, dynamics are even more complex as the turbine moves in response  
55 and in reaction to the incoming wind and wave variations. This introduces additional inertial and gravitational loading on many  
56 structural components (Jonkman and Matha, 2011). Thus, differences in rotor loading may influence the response of the system,  
57 indirectly influencing other component loads and amplifying the differences between the models.

58 The current study contributes to the field by presenting the outcomes of an extensive code-to-code comparison considering  
59 realistic environmental conditions and three different floating substructure designs. Environmental conditions from an existing  
60 European site are obtained using the procedure described in (Papi et al., 2022c) to obtain realistic distributions of wind speed,  
61 significant wave height, peak spectral period and wind-wave misalignment. The three test-cases - a spar-buoy, a semi-  
62 submersible and the innovative two-part floater concept; Hexafloat, recently proposed by Saipem - are simulated in a variety of  
63 Design Load Cases (DLCs), including both power-production and parked conditions, as well as wind gusts. The test-cases are  
64 simulated using three offshore codes, OpenFAST-~~(OF)~~, DeepLines Wind-~~(DL)~~ and QBlade-Ocean-~~(QB)~~, which was recently  
65 extended to enable offshore simulations within the Horizon 2020 project FLOATECH. The latter code includes higher-fidelity

66 modeling features such as LLFVW wake aerodynamics and explicit buoyancy calculation, as illustrated in (Behrens De Luna et  
67 al., 2023).

68 The predicted dynamics are compared in terms of extreme loads, fatigue loads and statistics. Time series are also compared in  
69 detail to give more insight into the differences in dynamics. The entire input conditions and compared datasets are available  
70 open-access and can act as validation databases for other offshore codes or as a benchmark for future modeling improvements.  
71 An extensive comparison, involving three different models with different substructure designs, three different numerical codes  
72 and multiple DLCs that include hundreds of simulations is an important point of novelty of this study and does not come without  
73 challenges. In fact, comparing coupled simulations that are aero-hydro-servo-elastic in nature such as in this study makes  
74 isolating the potential sources of any differences challenging. Nonetheless, it offers the unique opportunity of evaluating the  
75 trade-off between computational time and accuracy of the modeling theories in terms of their impact on the final design load  
76 predictions in a realistic scenario. It also allows one to highlight user-bias in the set-up of FOWT simulations. In this view, some  
77 critical aspects to consider during model set-up, that lead to significant differences in ultimate and fatigue loads in the compared  
78 models such as structural damping ratios and control strategy are discussed in detail.

79 This paper is organized as follows: In [Section-Sect. 2](#) the procedure required to set up the code-to-code comparison that is  
80 presented herein is detailed, starting from environmental conditions and continuing with DLC definition, test-case selection, and  
81 data post-processing. In [Section-Sect. 3](#) some details regarding the modeling theories underpinning the compared tools are given.  
82 In [Section-Sect. 4](#) the main results are presented, starting from a general statistical comparison of key metrics, and then moving  
83 to the comparison of design-driving extreme and fatigue loads. The principal results are discussed, and the conclusions drawn  
84 in [Section-Sect.5](#)

## 85 **2 A Procedure for Code-to-Code Comparison of FOWTs in Realistic Environmental Conditions**

86 The set-up of a design load calculation of a FOWT is a complex task on its own. Expertise is required in the selection and set-  
87 up of relevant DLCs in compliance with the various international standards (International Electrotechnical Commission, 2019;  
88 DNVGL, 2016). In the case of FOWTs, expertise is also required in the selection of environmental conditions to use, which are  
89 site dependent. Finally, a full load calculation can produce thousands of hours of time series data, and data processing techniques  
90 are required to make it more manageable and useful for the design process. In the context of this study, all these aspects will be  
91 briefly presented as they have already been touched upon in two publications by the authors (Papi et al., 2022c; Papi and  
92 Bianchini, 2023), that will be referenced later on in this [Section](#) where appropriate.

### 93 **2.1 European Met-Ocean Conditions**

94 Design classes are not currently prescribed for any type of offshore wind turbine as they are for onshore wind turbines, in favor  
95 of standardization. Although the need for such standardization is acknowledged and encouraged in the DNVGL-SST-0119  
96 design standard (DNVGL, 2018), the designer is currently required to verify the turbine and substructure combination of choice

97 for specific installation sites. As discussed in the following [Sections](#), standards require the definition of specific wind conditions,  
98 normally grouped in “models” such as the Normal Turbulence Model (NTM), and sea condition, generally grouped in “sea  
99 states”. Some databases containing such met-ocean data can be found in previous work – for a comprehensive literature review  
100 see (Papi and Bianchini, 2023) – however if we restrict our research to Europe, we did not find suitable met-ocean conditions  
101 for this analysis. Therefore, an open-source procedure to obtain and prepare long-term environmental data so it can be used in a  
102 design load calculation of an offshore wind turbine was developed. The procedure that is detailed in (Papi et al., 2022c) and is  
103 available open-access for others to use and improve upon (10.5281/zenodo.6972014).

104 Data is obtained from the Copernicus re-analysis database ERA5. Environmental data is available on a 30x30 km grid, therefore  
105 the procedure can be applied to a generic world-wide offshore site. In this study, hourly records of wind speed, wind direction,  
106 significant wave height, wave direction and peak spectral period from 1979 to 2000 for a site located west of the Scottish island  
107 of Barra are used. This location was chosen because of its particularly harsh environment, expected to increase non-linearities  
108 and differences in the examined models, and because it is also used in other EU-funded projects such as LifeS50+ (Antonia  
109 Krieger et al., 2015) and CoreWind (Vigara et al., 2020). Although more research would be needed to properly support this  
110 claim, due to the severity of the considered met-ocean conditions, it is reasonable to believe that any differences between the  
111 codes represent an upper limit, and smaller differences are likely to be found in less demanding conditions.

112 The open-source Python tool Virocon (Haselsteiner et al., 2019) is leveraged to build a joint probabilistic model of the dataset,  
113 able to describe the long-term probability of the four environmental variables that are considered: wind speed ( $U_w$ ), significant  
114 wave height ( $H_S$ ), peak spectral period ( $T_p$ ) and wind-wave misalignment ( $M_{ww}$ ). The model is then used to find the most likely  
115 combination of  $H_S$  and  $T_p$  for a given  $U_w$ , defining the Normal Sea State (NSS), and to define environmental contours: extreme  
116 conditions with 50-year recurrence period that are used to define the Extreme Sea State (ESS) and the Severe Sea State (SSS).  
117 More details on how these sea states are defined are summarized in (Papi et al., 2022c), while information on environmental  
118 contours and their applications to offshore wind turbines can be found in (Haselsteiner et al., 2020, 2021; Valamanesh et al.,  
119 2015).

## 120 2.2 DLC Selection and Environmental-Simulation Conditions

121 Code-to-code comparisons in a variety of environmental conditions are performed in this study. As such, simulations in various  
122 met-ocean conditions are performed. The specific combination of met-ocean condition and operating condition is a Design Load  
123 Case (DLC). In this study normal operating conditions and parked DLCs are simulated, as shown in Table 1. , While this  
124 paragraph contains a general overview of the selected DLCs, a more detailed explanation of the selected process can be found  
125 in the FLOATECH project deliverables (Papi et al., 2022a, b), and in (Papi and Bianchini, 2023). To obtain representative  
126 ultimate loads, operation in extreme turbulence (DLC 1.3), in severe seas (DLC 1.6) and during an extreme operating gust with  
127 direction change (DLC 1.4) are considered. In these load cases, wind and waves are considered aligned as a worst case scenario,  
128 in compliance with international standard prescriptions (IEC TS 61400-3-2:2019 | IEC Webstore, 2023). In, as well as the DLCs  
129 where the turbine is being parked during in one year (DLC 6.3) and fifty years extreme environmental conditions, with (DLC 6.2)

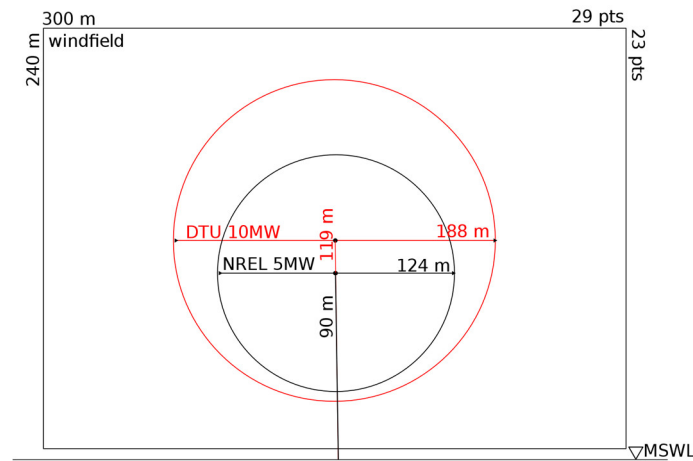
and without (DLC 6.1) grid loss, a  $\mp 30^\circ$  wind-wave misalignment is also considered. ~~With the exception of DLC 1.4, where simulations are 10 minutes long. All in all the other~~ ultimate load DLCs simulations are one hour long-, ~~with the exception of DLC 1.4, where simulations are 10 minutes long. In this DLC, interest is put on the extreme loads caused by the transient wind gust. As such, these simulations can be shortened without loss of relevant information.~~ Moreover, multiple turbulent seeds and yaw misalignments are considered within each DLC. For fatigue loads, normal operation in normal inflow and sea conditions (DLC 1.2) is considered. In this DLC, in accordance with indications coming from design standards (International Electrotechnical Commission, 2019), that require the full design space to be explored, multiple sea states are examined, including multiple combinations of the four environmental variables. Therefore, the design space is divided into bins, and at least one model evaluation for each bin is required. To keep the number of simulations manageable in the context of a code-to-code comparison endeavor, two strategies to reduce the number of required model evaluations are adopted. Both strategies were proposed in (Stewart, 2016); the first is the “probability sorting method”, where the least likely bins are discarded as these conditions are unlikely and are expected to have little impact on fatigue loads. In this study the most likely bins, ensuring a total combined probability of 90% are kept in the analysis. The second strategy is bin coarsening, in which the width of the bins is increased, thereby reducing their number. As discussed in (Papi and Bianchini, 2023), by combining the two strategies a relatively manageable number of bins is obtained: 252. For each bin two half-hour simulations are performed with different yaw misalignments.

**Table 1: DLCs used in this study. Normal operating conditions in various sea states and turbulence levels in DLCs 1.2 to 1.6 for the evaluation of fatigue (F) and ultimate (U) loads. In DLCs 6.1 to 6.3 the FOWTs are parked in extreme conditions. In DLC 6.2 a grid loss scenario is modelled, and thus multiple values of yaw-error are considered. Acronyms are described in nomenclature list.**

DLC	wind		waves			dur. [s]	seeds/ws	yaw	n° ws	sims	type	
	model	speed	model	height	period							dir.
<b>1.2</b>	NTM	$V_{in}-V_{out}$	NSS	-	-	MUL	1800	1	0, 10°	11	504	F
<b>1.3</b>	ETM	$V_{in}-V_{out}$	NSS	$E[H_S V_{hub}]$	$E[T_P H_S]$	COD	1800	9	0, $\mp 10$	11	99	U
<b>1.4</b>	ECD	$V_r \mp 2$ m/s	NSS	$E[H_S V_{hub}]$	$E[T_P H_S]$	COD	600	-	0	6	12	U
<b>1.6</b>	NTM	$V_{in}-V_{out}$	SSS	$H_S$ , SSS	$E[T_P H_S]$	COD	3600	9	0, $\mp 10$	11	99	U
<b>6.1</b>	EWM50	$V_{50}$	ESS	$H_{S50}$	$E[T_P H_S]$	0°, $\mp 30^\circ$	3600	2	0, $\mp 10$	1	12	U
<b>6.2</b>	EWM50	$V_{50}$	ESS	$H_{S50}$	$E[T_P H_S]$	<u>0°, <math>\mp 30^\circ</math></u>	3600	2	0,45,90 135,180	6	12	U
<b>6.3</b>	EWM1	$V_1$	ESS	$H_{S1}$	$E[T_P H_S]$	0°, 30°	3600	2	0, $\mp 20$	1	12	U

To ensure a fair comparison between the codes an attempt was made to match environmental inputs as well as possible in the numerical models. The wave time series are generated in DeepLines and then imported in OpenFAST and QBlade, while the

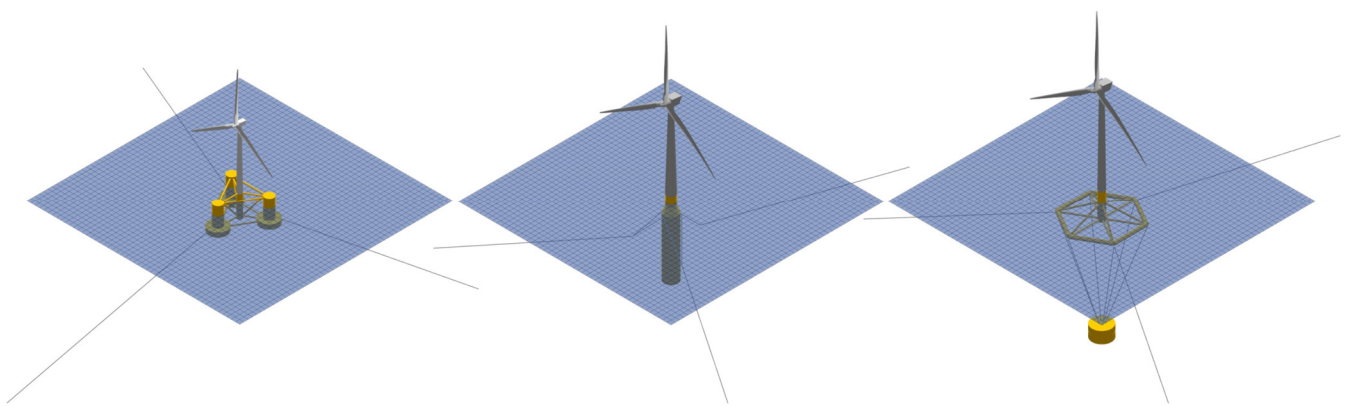
153 wind fields are generated by each participating institution using the same TurbSim (Jonkman, 2014) settings. The same wind  
154 fields are used in all three test cases, as if they were installed in the same site, regardless of the rotor size used. Therefore, the  
155 larger 10MW rotor defines the overall size of the wind field. A schematic representation of the wind fields is shown in Fig. 1.  
156



157  
158 **Figure 1: Schematic illustration of the wind field dimensions as used in this study with respect to the NREL 5MW and DTU 10MW**  
159 **rotors. The same wind fields are used on all three test-cases regardless of rotor size.**

### 160 2.3 Considered FOWT Designs

161 For the sake of generality and completeness of the analysis three floating turbine concepts are analyzed. Each test case features  
162 a different floating platform concept, namely a semi-submersible, a spar-buoy and Hexafloat. The three concepts are all derived  
163 from those in (Perez-Becker et al., 2022; Behrens De Luna et al., 2023), where some calibration was required to properly align  
164 the models with the experiments. The main characteristics of the three test-cases are detailed in the following.



165  
166 **Figure 2: Illustration of the examined numerical models in QBlade-Ocean. From left to right: NREL 5MW OC4, DTU 10MW**  
167 **Hexafloat-Softwind and DTU 10MW SoftwindHexafloat.**

168

### 169 **2.3.1 NREL 5MW OC4 DeepCwind**

170 The NREL 5MW OC4 semi-submersible FOWT (hereafter OC4) is an open-access turbine model defined in (Robertson et al.,  
171 2014a), upon which many code-to-code comparison exercises are based (Robertson et al., 2014b, 2017). It makes use of the  
172 NREL 5MW RWT rotor (Jonkman et al., 2009), representative of a utility-scale multi-MW rotor. The rotor is mounted on the  
173 DeepCwind semisubmersible floating platform. The platform was developed with the aim of generating test data for use in the  
174 validation of FOWT modeling tools.

175 The same tower design that was developed for use on the OC3-Hywind spar platform (Jonkman, 2010) is used. The semi-  
176 submersible floater consists of a main central column connected to the tower and three side columns spaced  $120^\circ$  apart. The  
177 offset columns are larger at the base, acting like heave plates to control the vertical motion of the FOWT and are connected  
178 together through a series of braces. A catenary mooring system is used. Three  $120^\circ$  lines are used to anchor the turbine to the  
179 seabed with one mooring line pointing directly upwind and the other two downwind.

### 180 **2.3.2 DTU 10MW Softwind**

181 The DTU 10 MW Softwind spar FOWT (hereafter Softwind) is a 1:40 scale floating platform designed by École Centrale de  
182 Nantes to develop, demonstrate, and validate a Software in the Loop (SiL) approach whereby an actuator is used to simulate the  
183 aerodynamic forcing at model scale in place of a scaled rotor. The model and experiments are described in (Arnal, 2020). The  
184 rotor nacelle assembly (RNA) is described in (Bak et al., 2013). With respect to the models used in (Behrens De Luna et al.,  
185 2023) that mimic the characteristics of the experiments (Arnal, 2020), some changes were implemented to increase the robustness  
186 of the numerical simulations when using the realistic met-ocean conditions considered in this work. Namely, the tower was  
187 stiffened, moving to a stiff-stiff design to avoid wave and 3P tower resonance. The tower designed by Olav-Olsen<sup>1</sup> in the  
188 LifeS50+ project for the OO-Star floater is used (Borg, 2015; Yu, n.d.). Notably this tower is heavier than the one used in the  
189 Softwind test campaign. The mass distribution in the floater is also changed. In order to have a realistic mass distribution and  
190 inertial properties, we hypothesized the use of high-density ballast in the spar body, thus lowering the Center of Gravity (CoG)  
191 with respect to the scaled model used in the experiments, which housed control electronics and batteries within the buoy. The  
192 mass of the floater is also lowered by approximately 2% to compensate for the heavier tower and maintain approximately the  
193 same draft. Furthermore, lowering the CoG lowers the platform pitch natural period, allowing for the use of a faster controller,  
194 as explained in [Section-Sect. 3.3](#). The specific changes are detailed in (Papi et al., 2022a). This modified floater design is not  
195 intended to be built and is only meant for numerical comparisons using a realistic design that is also numerically stable. These  
196 changes are therefore deemed appropriate for the goal of this study.

---

<sup>1</sup> The OO-Star Wind Floater has been developed by Dr. Techn. Olav Olsen (OO) since 2010 and is the property OpenFAST Floating Wind Solutions AS. OO has approved that the public model from LifeS50+ can be used for the research activities within FLOATECH. The model shall not be used for other purposes unless it is explicitly approved by OO.



197 In DeepLines, after unsuccessful initial attempts to align the model to QBlade and OpenFAST, and, in an initial phase, to the  
198 Softwind experiments (Arnal, 2020), a different tuning approach was employed for the hydrodynamics of the model. In  
199 particular, the pitch and roll inertias of the floater were decreased to better align the respective natural frequencies in free decay  
200 tests, and additional added mass on the spar buoy was introduced through Morison's equation to improve the agreement during  
201 surge free-decay tests. Lastly, mooring line tension was lowered to better align with the experimental data. A full description of  
202 the differences can be found in (Papi et al., 2023).

### 203 **2.3.3 DTU 10MW Hexafloat**

204 The DTU 10MW Hexafloat FOWT (Hereafter Hexafloat) consists of the DTU 10MW RWT mounted to the Hexafloat floater  
205 concept proposed by Saipem. As shown in Fig. 2, the substructure consists of a floater made of relatively slender steel braces  
206 connected to a counterweight by six tendons. This floater configuration did not require changes to the tower design and therefore  
207 the standard onshore tower of the DTU 10MW RWT (Bak et al., 2013) is used. This model is in effect identical to the one used  
208 and described in (Perez-Becker et al., 2022; Behrens De Luna et al., 2023)

### 209 **2.4 Post-Processing and Data Management**

210 The raw time series data obtained for the three models is post-processed using open-source tools, namely MLife (Hayman, 2012)  
211 and MExtremes (Buhl, 2015) developed by NREL. The main sensors that are compared in the study are shown in Tab. 1 and  
212 consist of blade root and tower base bending moments, mooring line fairlead tensions, nacelle fore-aft acceleration, control  
213 signals and platform motions. Some of these sensors act like a proxy to compare the influence of various physical phenomena  
214 on loads, such as nacelle acceleration that is used to gauge inertial loads on the tower and platform pitch that is used as indication  
215 of gravitational tower loading. The mechanisms that relate platform motions and substructure loading are discussed in (Robertson  
216 and Jonkman, 2011; Papi and Bianchini, 2022) and will only briefly be explained throughout this work where necessary.

217 MLife is used to compute Damage Equivalent Loads (DELs). DELs are the cyclic load amplitudes that cause the same fatigue  
218 damage to the structure over a certain number of cycles as the time series of a given load sensor. The Palmgren-Miner linear  
219 damage accumulation hypothesis is used to derive DELs, which can therefore only be considered representative equivalent loads  
220 if this hypothesis is valid. In this study zero-mean DELs are considered, and thus the mean of each loading cycle is disregarded.  
221 1Hz DELs give the equivalent damage during one simulation, while lifetime DELs represent the equivalent damage over the  
222 entire lifetime of the turbine. They can be conceptually thought of as a combination of 1Hz DELs weighted by their respective  
223 probability of occurrence, which in this case is a distribution that depends on the four environmental variables defined in [Section](#)  
224 [Sect. 2.1](#). As shown in Tab. 1, only the simulations in DCL 1.2 are used to compute DELs.

225 MExtremes is used to compute ultimate loads on the structure. In this case, DLCs 1.3, 1.4, 1.6, 6.1, 6.2 and 6.3 are used. To  
226 obtain a conservative estimate of ultimate loads in accordance with IEC 61400-1 annex I (International Electrotechnical  
227 Commission, 2019), an averaging approach is used when computing ultimate loads, as explained in (Buhl, 2015).



**Table 1: Sensors considered in the analysis.**

Sensor	OpenFAST ref. sys.	Name	Type
Blade root in-plane/out-of-plane bending moment	Coned CS <b>c</b>	B# M <sub>x</sub> / B# M <sub>y</sub>	F/U
Tower base fore-aft/side-side bending moment	Tower base CS <b>t</b>	TB M <sub>y</sub> /TB M <sub>x</sub>	F/U
Mooring line fairlead tensions	-	T ML#	F/U
Nacelle fore-aft acceleration	Tower top CS <b>p</b>	Nac. TAx	U
Control signals (blade pitch, gen. torque, rotor speed)	-	$\theta, \tau, \Omega$	-
Platform motions (computed @SWL)	Platform CS	surge, sway, pitch, etc...	-

### 229 3 Methods

230 This work leverages some of the authors' past experience and as such many of the same modeling techniques as described in  
 231 (Behrens De Luna et al., 2023) are used, where a more complete description of the employed methods can be found. Three  
 232 distinct numerical tools are used in this code-to-code comparison: OpenFAST v3.0, DeepLines Wind<sup>®</sup> and QBlade-Ocean. The  
 233 tools have been compared to experimental results on scaled models and have shown, after adequate model tuning, good ability  
 234 to capture the behavior of the different systems. The results of this modeling and validation effort are discussed in (Perez-Becker  
 235 et al., 2022; Behrens De Luna et al., 2023). The main numerical models in each code are described in this [sSection](#).

#### 236 3.1 Aerodynamic Models

237 All the models compared herein use low- to medium-fidelity aerodynamic models. The blade aerodynamics are not explicitly  
 238 modeled. Instead, a series of 2D aerodynamic coefficients is used in their place. Corrections to account for 3D flow effects are  
 239 built into the aerodynamic coefficients for all the models. Moreover, Gonzalez's variant of the Beddoes-Leishman dynamic stall  
 240 model (Leishman, 2016; Damiani and Hayman, 2019) is used in OpenFAST. In QBlade dynamic stall is modeled using Øye's  
 241 model (Marten, 2020), while in DeepLines no unsteady airfoil aerodynamics are accounted for. The relative velocities acting  
 242 on the blades are determined by the wake model. A Dynamic Blade Element Momentum (DBEM) wake model is used in  
 243 OpenFAST and DeepLines, where the rotor is divided into a series of radial and azimuthal streamtubes and for each streamtube  
 244 a momentum balance is performed. More details on BEM models can be found in (Burton, 2001; Hansen, 2008), and details  
 245 regarding the specific DBEM model implemented in OpenFAST are in (Ning et al., 2015; Branlard et al., 2022). These models  
 246 have been the industry workhorse for decades and although very simple, they have been extended in time through the addition  
 247 of empirical sub-models and now fully qualify as engineering models. A higher-order Lifting Line Free Vortex Wake (LLFVW)  
 248 model is used in QBlade. Here, the wake is modeled as a series of vortex filaments. Wake nodes are advected downstream by  
 249 the incoming wind speed and the cumulative induction of all wake filaments. More details on these models and how they are  
 250 implemented in QBlade can be found in (Van Garrel, 2003; Marten et al., 2015). The same aerodynamic lift and drag tables are

251 used in all three codes for both aerodynamic models and correspond to the public definitions of the NREL 5MW and DTU  
252 10MW rotors.

### 253 3.2 Structural Models

254 Structural dynamics are modeled with a modal-based linear superposition approach in OpenFAST through the submodule  
255 ElastoDyn. One limitation is that blade torsion is not modeled in ElastoDyn. In QBlade and DeepLines on the other hand, a  
256 higher fidelity finite-element approach is used, whereby the structural dynamics are modeled with a multi-body representation  
257 that uses Euler-Bernoulli beam elements in a co-rotational formulation (Marten, 2020; Le Cunff et al., 2013). Within OpenFAST  
258 a more sophisticated blade structural model exists that is able to account for blade torsion. Nonetheless, it was chosen to use  
259 ElastoDyn in this study for two reasons. The first reason is to speed up the OpenFAST calculations, as ElastoDyn requires less  
260 computational resources to run. The second reason is that by using a simpler structural model in OpenFAST, the impact of  
261 ~~structural modeling accuracy can be better~~this choice on the global dynamics and loads of the chosen floating systems can be  
262 evaluated.

### 263 3.3 Control

264 In all three models the ROSCO v2.4.1 open-source controller (Abbas et al., 2022) is used. This controller has been selected as it  
265 is open-source and it includes an automatic tuning toolbox that can be used to determine the proportional and integral gains of  
266 the blade pitch controller in a simple manner (Lenfest et al., 2020). A traditional  $K\omega^2$  law is used for the torque controller below  
267 rated wind speed. Above rated wind speed constant-torque control strategy is used. The pitch controller gains are tuned using  
268 ROSCO controller's automatic pitch-tuning routine based on the OpenFAST models of the two rotors. The controller includes  
269 a nacelle-velocity feedback loop developed especially for FOWTs, with the objective of avoiding negative blade-pitch controller  
270 damping that can occur in the case of FOWTs. However, this feature is not used in this study. The reason for this being that the  
271 feature did not work for the DeepLines models, as the required nacelle velocity sensor was not available as a controller input in  
272 this code. In order to have a fair comparison between all codes, we decided to disable this feature and instead tuned the pitch  
273 controller to have lower PI-feedback terms. The natural frequencies and damping ratios of the pitch controller used for the three  
274 models are shown in Table 2. For all three models the natural frequency of the blade pitch controller is set below the platform  
275 pitch natural frequency, mitigating possible controller-driven system instabilities. Despite this, a certain degree of blade pitch-  
276 induced platform motion is noted, especially in the Softwind test-case, at near-rated wind speeds. The phenomenon impacts  
277 QBlade simulations more than OpenFAST and DeepLines simulations. The reason for this difference is probably linked to slight  
278 differences in the aerodynamic models that cause different controller reactions-, as explained in detail in Sect. 4.3.1. More  
279 research needs to be done to fully understand these differences.  
280 In the OC4 model, a peak-shaving minimum pitch saturation schedule is considered. Peak shaving is used to reduce loads near  
281 rated wind speed by imposing a minimum pitch angle as a function of the low pass filtered wind speed at hub height, as explained

282 in (Abbas et al., 2022). In this model the same settings are used as in the public example that can be found in the ROSCO  
283 repository.

284 In DLC 1.4 shut-downs are performed by overriding the blade pitch controller with a specified pitch to feather maneuver in each  
285 code. The pitch to feather maneuver is initiated 5 seconds after the wind gust peak, as if the controller was reacting to the  
286 detection of an extreme yaw error and the blades are pitched at a speed of 10 °/s. In DeepLines the pitch to feather maneuver is  
287 longer in duration due to a setup difference. In fact, a specific pitch rate during a pitch to feather override maneuver cannot be  
288 specified in DeepLines, which needs a start and end time of the operation. Therefore, depending on the initial blade pitch angle,  
289 which depends on the coupled simulation and is thus different for each turbulent seed and each code, this can result in different  
290 pitch rates.

291 **Table 2: Controller natural frequencies and damping ratios for the three test-cases.**

Model	Nat. f ( $\omega$ )	Damping ratio ( $\beta$ )
NREL 5MW OC4	0.2 [rad/s]	1 [-]
DTU 10MW Softwind	0.14 [rad/s]	1 [-]
DTU 10MW Hexafloat	0.114 [rad/s]	1 [-]

### 292 3.4 Hydrodynamics

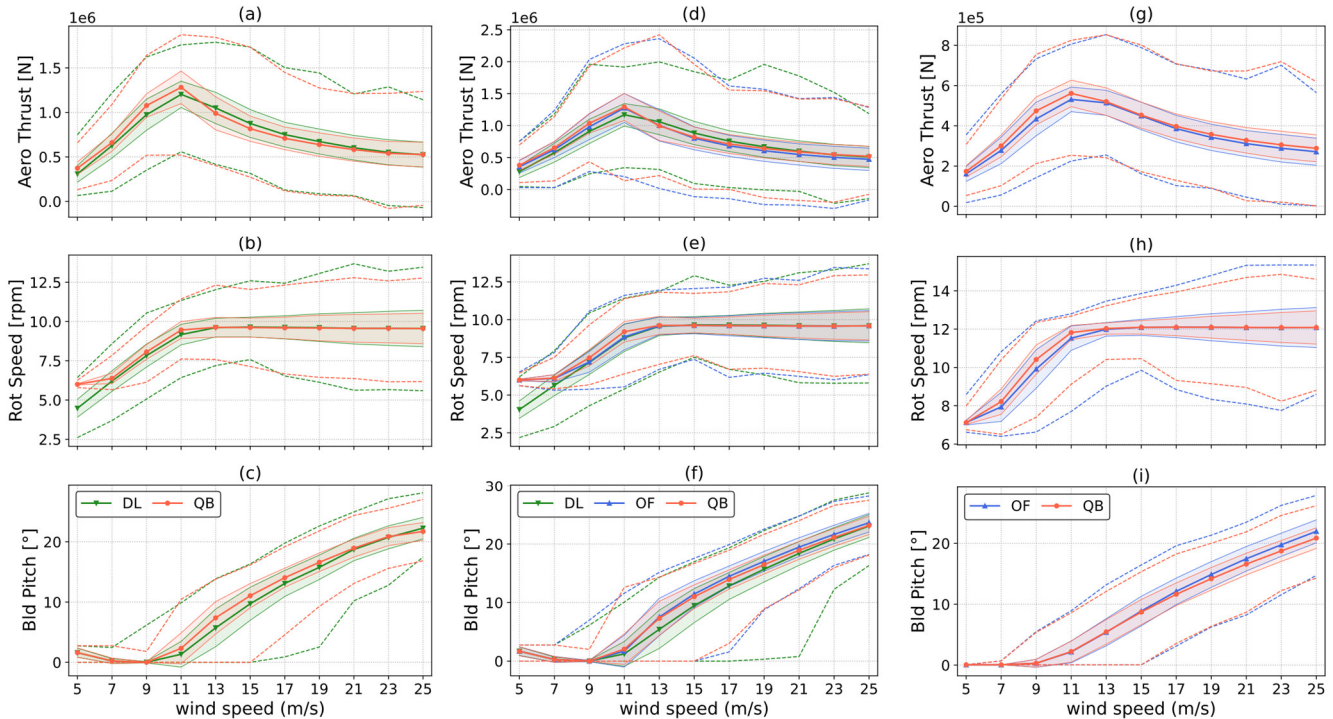
293 For the OC4 and Softwind designs a ~~Linear~~-Potential flow with Morison Drag (~~LPFMD~~) approach is used in both OpenFAST  
294 and QBlade, whereby hydrodynamics are modeled by combining a potential flow solution with quadratic drag computed with  
295 Morison's equation (ME). Full difference-frequency Quadratic Transfer Functions (QTFs) are used in both QBlade and  
296 OpenFAST in the OC4 design. They were computed and provided for this geometry by ECN using NEMOH (Kurnia et al.,  
297 2022), a potential flow hydrodynamic solver developed by ECN. On the Softwind design, quadratic hydrodynamic excitation  
298 forces are included with Newman's approximation (Faltinsen, 1993). The same hydrodynamic coefficients are used for each  
299 design in all three models. Buoyancy is modeled differently in the three codes: QBlade and DeepLines model this force explicitly.  
300 The spar structure is divided into a series of cylindrical sections and buoyancy forces are discretely applied. OpenFAST on the  
301 other hand models buoyancy force as constant term and a linear stiffness matrix to include the contributions of buoyancy to the  
302 restoring forces on the platform. Moreover, QBlade is able to model Wheeler wave stretching, which may introduce additional  
303 non-linear forcing. In the Hexafloat model a different approach is used. In fact, the floater is made of relatively slender braces  
304 that can be adequately modeled with a ME approach (Faltinsen, 1993). The same added mass and drag coefficients in both the  
305 axial and transversal directions are used in DeepLines and QBlade, and the hydrodynamic forces predicted by the two codes  
306 match well (Perez-Becker et al., 2022). The improvements implemented in QBlade to capture the slow-drift hydrodynamic forces  
307 described in ((Behrens De Luna et al., 2023), Sect. 3.4), are not used in this study, and all three models share the same basic  
308 hydrodynamic model, with the respective differences highlighted in this Section.

310 In this **S**section the most relevant results are presented. General statistical information is presented first, followed by a selection  
311 of ultimate loads recorded in DLCs 1.3 – 6.1 (Table 1) and a selection of lifetime DELs to compare fatigue load predictions. The  
312 Softwind design is used as the design of choice in most cases as it features all three codes, and results from the other two designs  
313 are also discussed when necessary. We were unable to complete all the simulations in all three codes in the comparison due to  
314 numerical convergence issues. In particular, one out of sixteen simulations in DLC 6.2 in the Softwind model was not completed  
315 in OpenFAST because of instabilities in the structural solver. Moreover, we were unable to complete all simulations in DLCs  
316 1.2 (498/504), 1.3 (86/99), 6.1 (12/18), 6.2 (12/16) and 6.3 (12/18) in DeepLines. Similar issues are also present in the Hexafloat  
317 model in DeepLines, where simulations did not converge in DLCs 1.2 (497/504), 6.1 (12/18), 6.2 (12/16) and 6.3 (12/18). The  
318 cause of the incomplete runs can again be traced back to numerical instabilities in the solution. We chose not to attempt re-  
319 running the simulations with a fine-tuning of the numerical solution scheme parameters because of budget and time constraints  
320 within the project. Therefore, while not an inherent limitation of the code, this result is what could be achieved by a prepared  
321 operator within the project timeline, which is also comparable to that of an industrial project. We were able to complete all the  
322 simulations in QBlade. Results have shown good agreement between the codes in DLCs where the machine is operating, but  
323 some discrepancies when the machine is parked. Moreover, generally larger differences in fatigue loads than in extreme loads  
324 between the codes are noted.

#### 325 **4.1 Statistical Comparison**

326 Figures 3 and 4 show a statistical comparison of selected operational sensors over the working range of the wind turbines. The  
327 wind speed is extracted at 100 m above mean sea water level. The markers represent the mean values recorded in DLC 1.2, the  
328 shaded area corresponds to twice the standard deviation of the signal for each wind speed and the dashed lines show the minimum  
329 and maximum values recorded during the DLC 1.2 runs. Control sensors, often used to monitor the operation of the wind turbine,  
330 are shown in Fig. 3. Although global trends are the same for all three codes in all three test-cases, some important differences  
331 can be pointed out. With respect to QBlade, mean aerodynamic thrust is lower for DeepLines in the Softwind and Hexafloat test  
332 cases at below rated wind speed and is also lower for OpenFAST in the OC4 test-case. In the case of the OC4 test-case, the  
333 difference in thrust can, at least partially, be attributed to differences in rotor speed (Fig. 3 (h)). In fact, mean rotor speed is  
334 higher in QBlade, causing the rotor to operate at a higher tip speed ratio (TSR), leading to a higher thrust coefficient. Similar  
335 differences in this regard were noted also in previous comparisons between QBlade and OpenFAST (Perez-Becker et al., 2020).  
336 For the Softwind and Hexafloat test-cases (Figs. 3 (b, e)), less difference in rotor speed can be noted, and the difference in thrust  
337 is therefore more likely to be caused solely by differences in the aerodynamic models. The differences in aerodynamic modeling  
338 are also apparent when analyzing blade pitch statistics in Figs. 3 (c, f, i). In fact, while good agreement in mean values can be  
339 noted for QBlade and OpenFAST, mean blade pitch is lower for DeepLines through most of the wind speed range. In addition,  
340 the difference between maximum and minimum blade pitch angles is larger for DeepLines respect to OpenFAST and QBlade.

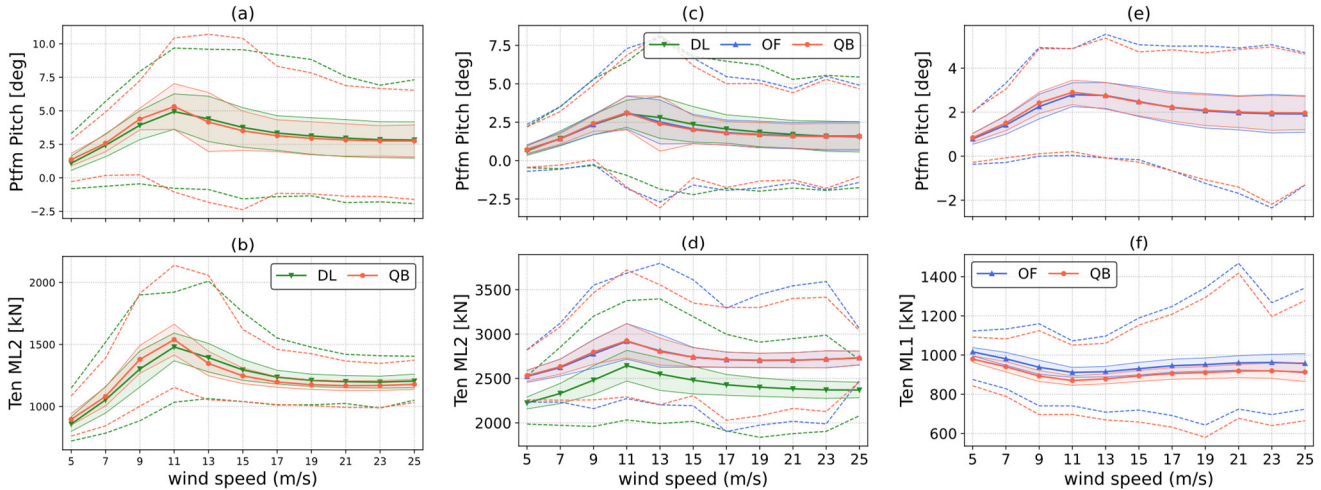
341 Moreover, as shown in Fig. 3 (b, e), ~~due to a compilation issue in the controller~~, minimum rotor speed is not enforced in  
 342 DeepLines, and the rotor operates at lower rpm at cut-in in both the Hexafloat and Softwind test cases. The ROSCO controller  
 343 that was used in this code-to-code comparison required recompiling to be used in DeepLines Wind because the blade pitch and  
 344 twist angle conventions that are used in this code differ from those used in QBlade and OpenFAST and as a result, minimum  
 345 rotor speed is not enforced in DeepLines. To the best of our knowledge, the controller is functionally identical to that used in  
 346 OpenFAST and QBlade in all other aspects. This influences fatigue loads, especially edgewise and in-plane blade root bending  
 347 moments, that are strongly dependent on cyclic gravitational loading. On the other hand, we can assume the influence of this  
 348 discrepancy on extreme loads to be limited, as these loads are recorded at higher mean wind speeds.



349  
 350 **Figure 3: Statistics of aerodynamic thrust (a, d, g), rotor speed (b, e, h) and blade pitch (c, f, i) as a function of mean wind speed**  
 351 **recorded in DLC 1.2. Solid lines with markers represent mean values, shaded areas represent twice the recorded standard deviation,**  
 352 **dashed lines for the minimum and maximum recorded values. DTU 10MW Hexafloat (a-c), DTU 10MW Softwind (d-f) and NREL**  
 353 **5MW OC4 (g-i).**

354 In Fig. 4, statistics of platform pitch and mooring line tension are shown. For the Softwind and Hexafloat test-case one of the  
 355 two upwind mooring lines is chosen, while for the OC4 test-case the tension of the upwind mooring line is reported in Fig. 4 (f).  
 356 As for the control sensors shown in Fig. 3, good general agreement can be seen for all three codes in all three test-cases. Platform  
 357 pitch is remarkably similar in mean value, standard deviation, and minimum/maximum value for the OC4 test-case (Fig. 4 (e)).  
 358 Very good agreement between OpenFAST and QBlade is also shown in Fig. 4 (a). At 13 m/s mean wind speed however, platform  
 359 pitch standard deviation is higher for QBlade. A similar trend can also be noted in Fig. 4 (c), where again the standard deviation

360 of blade pitch is higher for QBlade at 11 m/s and 13 m/s mean wind speeds. Analyzing the time series of the various codes at  
 361 these wind speeds reveals that the increased standard deviation is a result of blade pitch – platform pitch self-excitation. This  
 362 phenomenon is discussed in detail in [Section-Sect. 4.3](#). Mooring line tensions are in good agreement in all three test-cases  
 363 although some differences can be noted. The largest difference is shown in Fig. 4 (b), where a significant difference in mean  
 364 tension can be noted between DeepLines and the other codes. Such difference is a result of different model tuning, as discussed  
 365 in [Section-Sect. 2.3.2](#).



366  
 367 **Figure 4: Statistics of platform pitch (a, c, e), upwind mooring line tension (b, f) and tendon tension (d) as a function of mean wind**  
 368 **speed recorded in DLC 1.2. Solid lines with markers represent mean values, shaded areas represent twice the recorded standard**  
 369 **deviation, dashed lines for the minimum and maximum recorded values. DTU 10MW Hexafloat (a-b), DTU 10MW Softwind (c-d) and**  
 370 **NREL 5MW OC4 (e-f).**

371 **4.2 Ultimate Loads**

372 This section presents the ultimate loads, computed with the maximum averaging method described in [Section-Sect. 2.4](#), for key  
 373 selected load sensors. [This Section is focused on understanding which phenomena and modeling differences may influence the](#)  
 374 [prediction of extreme loads. The analysis focuses on maximum extreme loads only, disregarding minimum loads to streamline](#)  
 375 [the discussion. Minimum extreme loads are reported in Appendix A. In Fig. 5, the ratios of selected ultimate loads on the turbine](#)  
 376 [with respect to the values obtained in QBlade, assumed here as benchmark, are shown. The DLCs in which the respective](#)  
 377 [maximums are recorded are also reported for each of the bars in Fig. 5. For blade root bending moments, the maximum value](#)  
 378 [recorded across the three blades is shown. Figure 5 also reports the blade where the peak load is recorded. Ultimate loads are](#)  
 379 [recorded across all the DLCs, thus encompassing both power production and parked load cases, depending on the specific load](#)  
 380 [sensor and FOWT design being examined. In the OC4 test case \(Fig. 5 \(c\)\) extreme loads are predicted in the same DLC in](#)  
 381 [OpenFAST and QBlade, with the exception of blade root in-plane bending moment \(BR Mxc\). This FOWT design is the one](#)  
 382 [where the best overall agreement between the compared codes was reached. In the Softwind and Hexafloat designs, extreme](#)  
 383 [loads are recorded in different DLCs for some load sensors, as is the case for TT Fx for Softwind and BR Myc for Hexafloat. In](#)

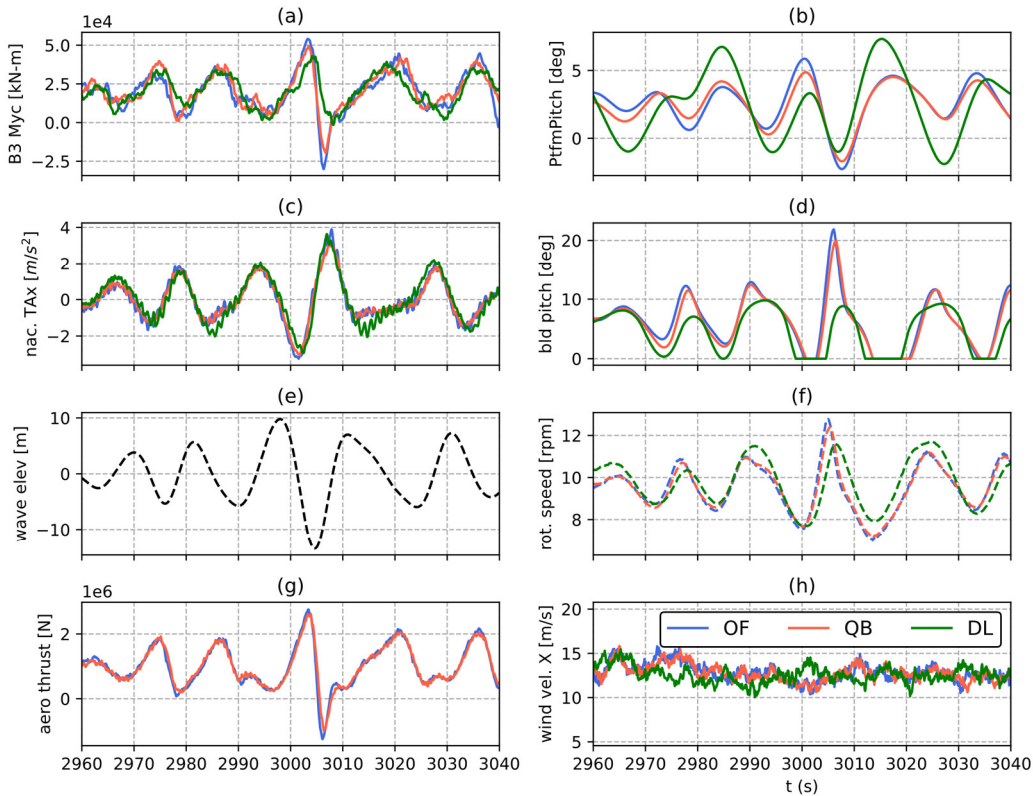
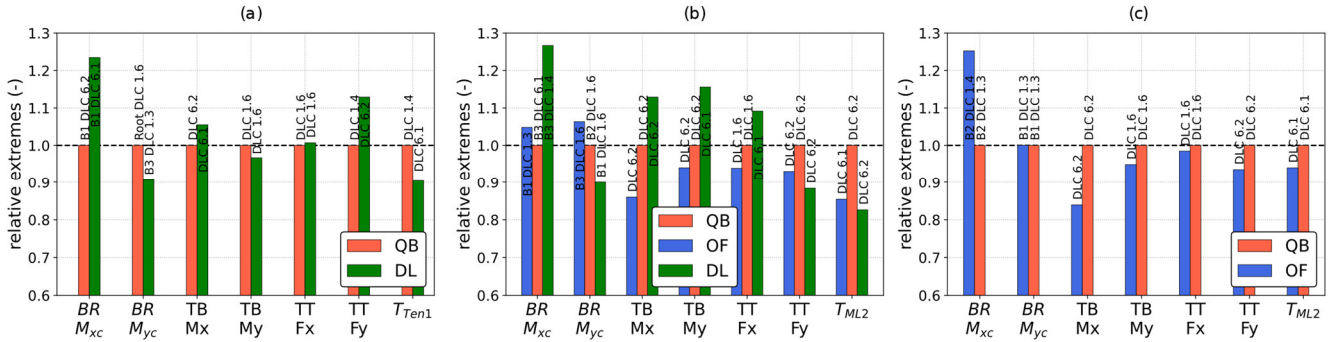


384  
385

both cases extreme loads predicted across multiple DLCs are very close in magnitude, causing the ultimate extreme load to be predicted in different DLCs depending on the specific model's response.

386  
387  
388

Figure 5: Selection of ultimate loads (maximum) recorded in the three simulation codes. (a) DTU 10MW Hexafloat, (b) DTU 10MW Softwind and (c) NREL 5MW OC4.



389  
390  
391  
392  
393

Figure 6: Time series of out-of-plane root bending moment of blade 3 of the Softwind model in DLC 1.6, ( $w_s = 11$  m/s,  $H_s = 9$ ), where maximum bending moment is recorded for OpenFAST. From top to bottom: B#3 out-of-plane root bending moment (a), platform pitch (b), nacelle fore-aft acceleration (c), blade pitch (d), and wave height at platform reference position (e), rotor speed (f), aerodynamic thrust (not available in DeepLines outputs) (g), wind speed at hub height (h).



#### 394 4.2.1 Blade Root Extreme Loads

395 Regarding blade root bending moments, there is larger variation in BR Mxc ultimate load than BR Myc. BR Myc is much higher  
396 in magnitude than BR Mxc and thus has a greater influence on component design. Nonetheless, BR Mxc is approximately 23%  
397 higher on the Hexafloat test-case for DeepLines, and 27% higher in the Softwind test-case. Similarly, BR Mxc is approximately  
398 25% higher for OpenFAST in OC4. Out-of-plane blade root bending moments are in better agreement, DeepLines predicting  
399 10% lower loads than QBlade in the Hexafloat and Softwind test-cases, while OpenFAST and QBlade are much closer, the  
400 former being 5% higher in Softwind and nearly identical to QBlade in OC4.

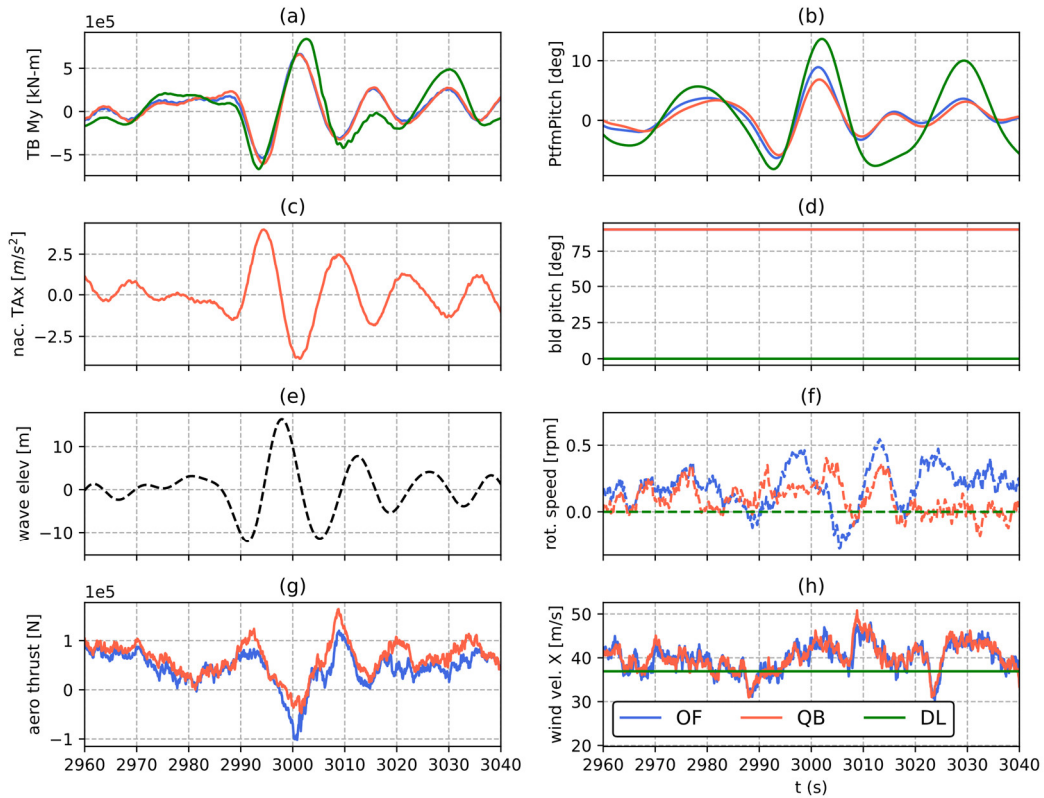
401 The out-of-plane blade root bending moments are mostly influenced by aerodynamic loading, as lift force is directed mostly out-  
402 of-plane. On a FOWT however, the coupled dynamics of the entire system influence these load sensors. This is demonstrated in  
403 Fig. 6, where the time series of multiple load sensors, including BR Myc, platform pitch, aerodynamic thrust and nacelle fore-  
404 aft acceleration are shown at the time instant where the maximum BR Myc in OpenFAST is recorded. When the load peak is  
405 recorded the wind speed is rising and is around the rated wind speed value. In addition, an extreme wave impacts the substructure.  
406 The latter causes the FOWT to move, as shown in the platform pitch and nacelle fore-aft acceleration sensors time series. In turn  
407 this causes large relative inflow variations on the rotor. As hydrodynamic forces cause the platform to swing forward, rotor thrust  
408 increases causing BR Myc to peak. Due to the increase in relative inflow, rotor speed increases (Fig. 6 (d)) and the controller  
409 reacts by aggressively pitching the blades, especially in QBlade and OpenFAST. While controller response depends on and  
410 influences the global response of the system, one reason for the different controller reactions in DeepLines is the different wind  
411 speed in this code (Fig. 6 (e)). In fact, the same wind fields are used in all three codes, but a time-shift is present in DeepLines  
412 with respect to the other models due to differences in how the wind fields are imported. In fact, depending on the simulation  
413 tool, wind fields are often shifted on import in order to make sure that the turbine is fully immersed in the wind field in case of  
414 yaw misalignment. On the other hand, no such shift is present in the wave fields. Therefore, environmental inputs are out of sync  
415 if OpenFAST and QBlade are compared to DeepLines. The increase in blade pitch is able to limit rotor speed overshoot but  
416 causes a sudden decrease in rotor loading, which in turn is the cause of BR Myc reaching a local minimum shortly after peaking.  
417 Therefore, platform motion influences BR Myc indirectly: not through variation in inertial and gravitational loads but through  
418 variation in aerodynamic loading. In summary, even small differences in aspects such as input conditions, hydrodynamics,  
419 aerodynamics, control, and overall set-up definition can influence ultimate loads through different system dynamic behavior.

#### 420 4.2.2 Tower Base Extreme Loads

421 Shifting focus to tower base loads, fore-aft (TB My) are, similarly to blade root loads, greater in magnitude than side-side loads  
422 (TB Mx) that will thus be treated briefly. Side-side tower base bending moment (TB Mx) ultimate load always occurs in parked  
423 conditions for all three test-cases and all three design codes. Moreover, except for DeepLines in the Hexafloat test-case, ultimate  
424 loads always occur in DLC 6.2, where in addition to +/- 30° incoming wave heading, yaw misalignment is present.

425 In all three test-cases a strong correlation between platform roll and TB Mx is present, indicating that these ultimate loads are  
426 hydrodynamics-driven. In fact, as the RNA and tower are heavy components, gravitational and inertial loads can be significant  
427 on FOWT towers. Regarding specific test-cases, in OC4 TB Mx ultimate load is approximately 16% lower in OpenFAST. This  
428 discrepancy is mainly caused by response at the tower natural frequency in QBlade, which is not present in OpenFAST. On the  
429 other hand, if time series of TB Mx are compared for the Softwind test-case, little variation can be noted between the three codes.  
430 For this load sensor the difference between QBlade and OpenFAST ultimate loads that is shown in Fig. 5, is amplified by the  
431 maximum averaging technique. As described in [Section-Sect. 2.4](#), the ultimate load in load cases with multiple turbulent seeds  
432 is computed as the maximum value closest to the mean of the maximums recorded across all the turbulent seeds. Therefore,  
433 because ultimate loads are slightly different in QBlade and OpenFAST, the peak load closest to the mean is recorded in different  
434 seeds for the two codes. This demonstrates how small differences between the models can be amplified by the post-processing  
435 technique.

436 Maximum tower base fore-aft bending moment (TB My) is also recorded in parked conditions in the Softwind test-case - DLC  
437 6.2 for QBlade and OpenFAST and DLC 6.1 for DeepLines. Analyzing the times series of TB My in DLC 6.1 (Fig. 7) when  
438 peak load is recorded in DeepLines, the ultimate load is generated by a combination of gravitational and inertial loading resulting  
439 from platform motion. Higher values of platform pitch are noted in DeepLines, possibly a result of the slacker mooring lines in  
440 DeepLines, which explain the higher TB My. On the other hand, in the Hexafloat and OC4 test-cases, maximum TB My is found  
441 in DLC1.6 for all codes ([Fig. 5](#)). In both the latter cases OpenFAST and DeepLines are approximately 5% and 3% lower than  
442 QBlade in this metric. In this case ultimate loads are recorded around rated wind speed, similarly to BR Myc. Differently from  
443 the latter, which is analyzed in detail in Fig. 6, in the case of TB My, platform motion contributes directly to tower base loading  
444 as it increases gravitational and inertial forces. Overall, the three codes are close in this metric confirming that all three are able  
445 to capture the system dynamics in presence of extreme waves to a similar degree.



446

447

448

449

450

**Figure 7: Time series of fore-aft tower base bending moment of the Softwind model in DLC 6.1, ( $w_s = 37$  m/s,  $H_s = 16.5$ ), where maximum bending moment is recorded for OpenFAST. Tower base fore-aft bending moment (a), platform pitch (b), nacelle fore-aft acceleration (c), blade pitch (d), and wave height at platform reference position (e), rotor speed (f), aerodynamic thrust (not available in DeepLines outputs) (g), wind speed at hub height (h).**

451

452

### 4.3 Fatigue Loads

453

#### 4.3.1 Blade Root Fatigue Loads

454

455

456

457

458

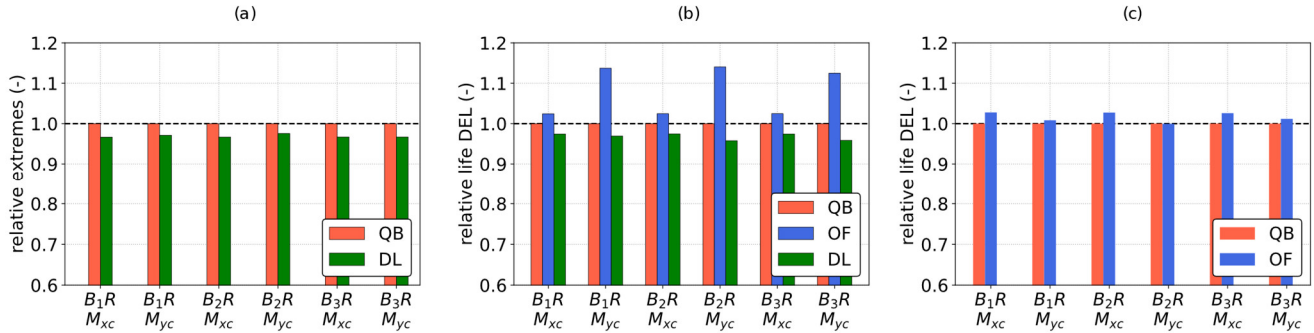
459

460

461

Lifetime, zero-mean DELs computed with the procedure highlighted in [Section Sect. 2.4](#) at blade root in the coned coordinate system are shown in Fig. 8. Contrary to extreme loads, a clear trend is apparent in this case. In fact, with respect to QBlade, Lifetime DELs are lower in DeepLines but higher in OpenFAST. In particular, 1Hz DELs are 3-5% lower than QBlade for DeepLines ~~in both the SW and HX test cases~~, with little variation across the three blades. Indeed, fatigue loads are consistent among the three blades for all three codes and all three test-cases, indicating good statistical convergence. Comparing QBlade and OpenFAST, blade root fatigue loads are very close (0-3%) in case of the OC4 test-case, while increases of up to 12% in out-of-plane blade root bending moments can be seen [for Softwind](#) ~~in case of the SW test case. In both OC4 and SW~~ [On the other hand](#), OpenFAST and QBlade are closer in the prediction of in-plane root bending moments than out-of-plane root bending

462 moments. The fatigue loads former are mainly driven by gravity, explaining the smaller differences between the compared wind  
 463 turbine simulation codes.



464  
 465 **Figure 8: Blade root fatigue loads in coned coordinate system: lifetime DELs normalized respect to values computed in QBlade. From**  
 466 **left to right: DTU 10MW Hexafloat, DTU 10MW Softwind and NREL 5MW OC4.**

467 The differences between the three models can be analyzed in more detail by comparing 1Hz DELs weighted by the probability  
 468 of each environmental condition to occur:

$$469 \overline{DEL}_t = p_t * DEL = p_t \left( \frac{\sum_j n_j A_j^m}{t} \right)^{1/m}$$

470  $p_t$  is the probability of each condition to occur,  $n_j$  and  $A_j$  are the combinations of rainflow counted  $j$  th number of cycles and  
 471 amplitude in each simulation and  $m$  is the Wöhlercurve exponent, equal to 10 for the composite blades and 4 for the other steel  
 472 components. As discussed in Section 2.4, 1Hz DELs multiplied by their respective probability of occurrence are representative  
 473 of the contribution to lifetime fatigue loads of each operating condition. Box plots of blade root bending moment weighted 1Hz  
 474 DELs for the SW test case are shown in Fig. 9. The boxes represent the 1<sup>st</sup> and 3<sup>rd</sup> quartiles, the whiskers indicate the data range,  
 475 the horizontal line is the median of the data and flier values are shown as scatter points. The weighted 1Hz DELs are grouped  
 476 by wind speed bin as this is the main environmental variable and is considered independent in the probabilistic hierarchical  
 477 model of the site (Section 2.1). This is apparent if the distribution of weighted 1Hz DELs are compared in case of B1R Mxc and  
 478 B1R Myc: high fatigue damage bins are shifted towards higher wind speeds in the latter with respect to the former, due to the  
 479 different dependency of 1Hz DELs with respect to the wind speed. In particular, BR Mxc 1Hz DELs depend strongly on  
 480 gravitational loads and are thus influenced by rotor speed, remaining fairly constant above rated. Therefore, normalized DELs  
 481 tend to decrease above rated as the probability of these wind speed bins decreases. On the other hand, BR Myc is influenced by  
 482 variations in aerodynamic load and thus 1Hz DELs relative to this load sensor continue to increase past rated wind speed, and  
 483 thus normalized 1Hz DELs are shifted to higher wind speeds with respect to Fig. 9 (a). Regardless of the considered bending  
 484 moment however, from a fatigue load perspective the most important cases are those with wind speeds between 9 m/s and 19  
 485 m/s, as they tend to show the highest weighted DELs.

486 Analyzing the differences between the three simulation codes, in the case of in-plane blade root bending moment, the same trend  
 487 can be noted at all wind speeds: QB 1Hz DELs are generally between the values assumed by OF and DL. The same can be said

when comparing OF and QB in the case of out-of-plane blade root bending moment. In this case 1Hz DELs are lower in DL only in the 11 m/s, 13 m/s and 19 m/s wind speed bins. However, given the large contribution of these wind speed bins to the blade root out of plane lifetime DEL, the latter are lower overall, as shown in Fig. 8.

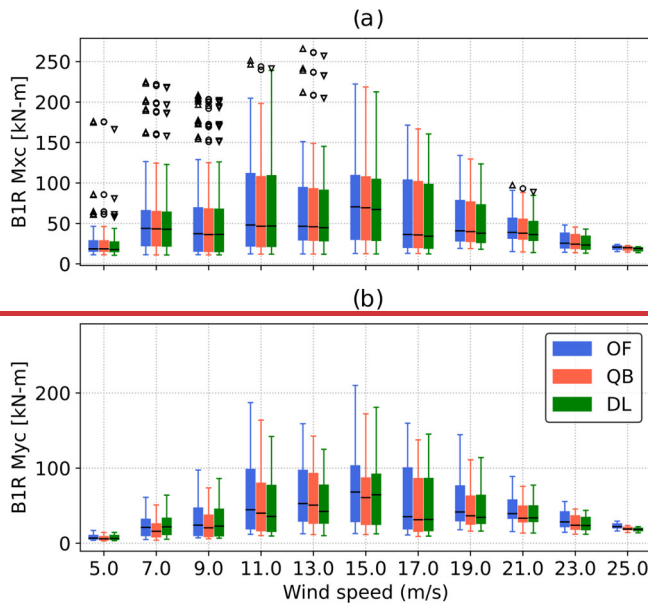


**Figure 9: Statistics of 1Hz zero-mean Damage Equivalent Loads weighted by the probability of each environmental bin they refer to for the SOFTWIND test case. The boxes represent the 1<sup>st</sup> and 3<sup>rd</sup> quartiles, the whiskers represent the data range and are found by adding/subtracting to the box edges 1.5 times the interquartile (IQR) range, the horizontal line is the median of the data and flier values are shown as scatter points.**

To better understand the differences in 1Hz-Lifetime DELs, the Cumulative Power Spectral Density (CPSD) of blade root bending moments for the Softwind FOWT design are shown in Fig. 10Fig. 9. They are obtained as the cumulative sum of the PSD of the signal. A CPSD plot is read from left to right; steps in the data indicate peaks in the underlying PSD. When comparing two signals, the increase or decrease in distance between the lines indicates the differences between them. The CPSDs for the Hexafloat FOWT design look very similar and are not shown here for brevity as similar conclusions can be drawn. At all three of the examined wind speeds (7 m/s, 13 m/s and 23 m/s) 1P loads are the main contributors to in-plane fatigue loading (BR Mxc). The magnitude of 1P excitation is lower in DeepLines for all three wind speeds. The most relevant differences in this regard can be seen at 7 m/s (Fig. 10Fig. 9 (a)) and can be explained by the difference in rotor speed that was noted in Fig. 3. Because minimum rotor speed is not imposed in DeepLines, while it is in QBlade and OpenFAST, the 1P peak spans a larger frequency range in the former and is lower in magnitude.

Differences are also present in the BR Mxc CPSD. The near absence of response between 1P and 2P, at wave frequency, indicates that apparent wind variations caused by platform motions do not induce relevant fatigue loading for this FOWT design. Three distinct phenomena drive the differences in this load sensor at the three wind speeds shown in Fig. 9. At 7 m/s (Fig. 10Fig. 9 (d))—At this wind speed OpenFAST and DeepLines show higher low-frequency excitation than QBlade. This phenomenon

510 deserves further attention and will be discussed later in this [Section](#) when similar results for the OC4 FOWT design are  
511 ~~noted~~[presented](#). Moreover, while small in magnitude when compared to low-frequency response, the 1P peak is larger in  
512 OpenFAST. 1P BR Myc load variation remains larger for OpenFAST across the wind speed range, ~~and higher peaks can be~~  
513 ~~noted also in~~[but are most noticeable at 23 m/s \(Figs. 10 \(e\)\) and \(f\)](#).  
514 ~~Especially at 23 m/s, OF's larger 1Hz DELs (Fig. 9) can mostly be attributed to differences in 1P response. In fact, low frequency~~  
515 ~~response is smaller for all three codes than it is at lower wind speeds, and so are the differences between the codes. Moreover, a~~  
516 ~~trace of response at the wave excitation frequency (below 1P) is only present in Fig. 10 (f). The near absence of response between~~  
517 ~~1P and 2P, at wave frequency, indicates that apparent wind variations caused by platform motions do not induce relevant fatigue~~  
518 ~~loading for this FOWT design. On the other hand, differences in the low frequency region are present at 13 m/s (Fig. 10 (e)),~~  
519 ~~where the predicted response in OpenFAST is larger. At this wind speed a large peak at the floater pitch natural frequency can~~  
520 ~~also be seen, especially for QBlade. As a consequence, BR Myc 1Hz DELs at 13 m/s computed with QB are similar to those~~  
521 ~~computed with OF, despite less load variation at 1P and at low frequencies. This peak in response at the floater natural frequency~~  
522 ~~is caused by blade pitch — floater pitch self excitation. As described in detail in (Larsen and Hanson, 2007), on a FOWT an~~  
523 ~~increase in blade pitch causes aerodynamic load to decrease, and the platform to swing forward as a consequence. In turn this~~  
524 ~~causes the apparent wind speed on the rotor to increase and rotor speed to follow. The controller will thus react to the increased~~  
525 ~~rotor speed by increasing blade pitch even further. A similar unstable behavior is triggered by a decrease in blade pitch, in this~~  
526 ~~case the platform swings backward, reducing apparent wind speed and rotor speed, promoting further blade pitch reductions. As~~  
527 ~~explained in Section 3.3, controller gains were reduced to avoid this phenomenon (see (Larsen and Hanson, 2007) for a detailed~~  
528 ~~explanation on the effectiveness of this strategy). Despite this, as confirmed by the increased platform pitch standard deviation~~  
529 ~~in Fig. 3, unstable behavior emerged at 13 m/s wind speed. This can be seen clearly in Figure 11. Here, the time series of platform~~  
530 ~~pitch and blade pitch for the three FOWT designs during a 13 m/s DLC 1.2 simulation that are shown. In Fig. 11, the OC4 model~~  
531 ~~is not affected by pitch self excitation, while the Hexafloat and Softwind models are. In the latter two models, DeepLines is the~~  
532 ~~least influenced by the phenomenon and QBlade is the most affected, despite all three codes using the same controller, proving~~  
533 ~~that differences between the models can lead to different controller actuation, and thus different ultimate and fatigue loads.~~

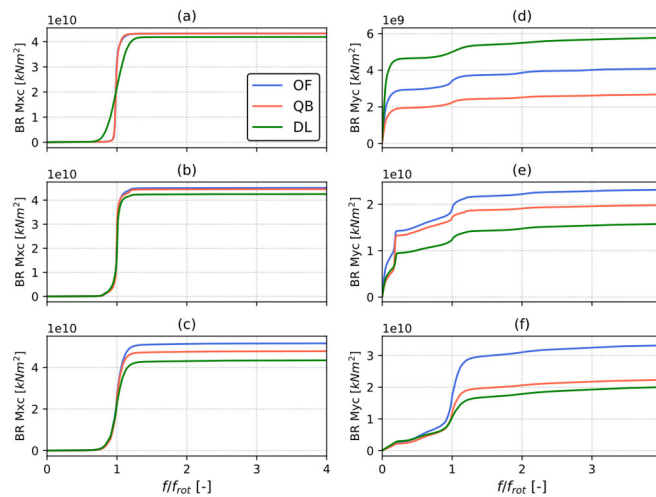
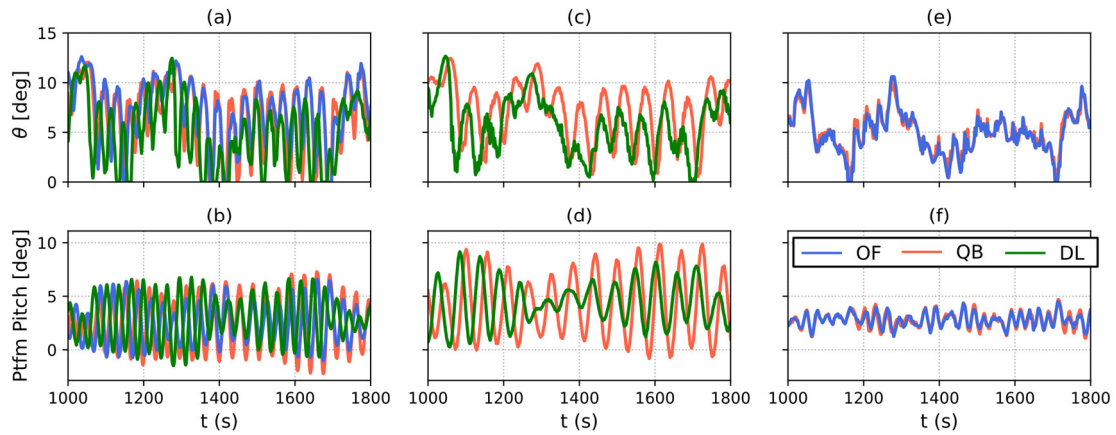


**Figure 9:** Cumulative Power Spectral Density (PSD) of blade root in-plane (a-c) and out-of-plane (d-f) bending moment for the Softwind test-case. Frequency is normalized by mean revolution frequency. PSD is computed on all simulations with 7 m/s (a, d), 13 m/s (b, e) and 23 m/s (c, f) mean wind speed.

Finally, at 13 m/s the three codes differ mainly in the low-frequency region, where the predicted response in OpenFAST is larger. Moreover, at this wind speed a large peak at the floater pitch natural frequency can also be seen, especially for QBlade. This peak in response at the floater natural frequency is caused by blade pitch – floater pitch self-excitation. As described in detail in (Larsen and Hanson, 2007), on a FOWT an increase in blade pitch causes aerodynamic loads to decrease, and the platform to swing forward as a consequence. In turn this causes the apparent wind speed on the rotor to increase and rotor speed to follow. The controller will thus react to the increased rotor speed by increasing blade pitch even further. A similar unstable behavior is triggered by a decrease in blade pitch, in this case the platform swings backward, reducing apparent wind speed and rotor speed, promoting further blade pitch reductions. As explained in Sect. 3.3, controller gains were reduced to avoid this phenomenon (see (Larsen and Hanson, 2007) for a detailed explanation on the effectiveness of this strategy). Despite this, as confirmed by the increased platform pitch standard deviation in Fig. 3 and blade pitch standard deviation in Fig. 4, unstable behavior emerged at 11 and 13 m/s wind speed. This can be seen clearly in Fig. 10, where the time series of platform pitch and blade pitch for the three FOWT designs during a 13 m/s DLC 1.2 simulation are shown - and also in Fig 17 (d) later on in this study. In Fig. 10, the OC4 model is not affected by pitch self-excitation, while the Hexafloat and Softwind models are. In the latter two models, DeepLines is the least influenced by the phenomenon and QBlade is the most affected, despite all three codes using the same controller.





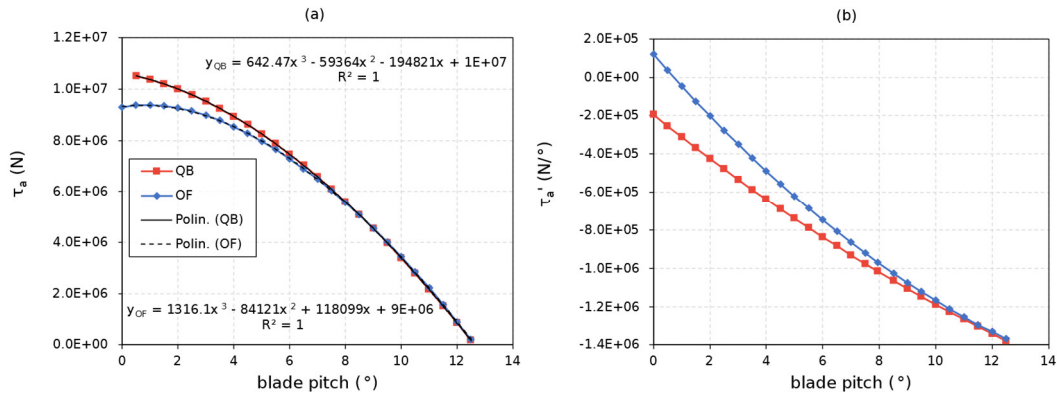
553  
554 **Figure 10:** Time series of blade pitch (top row) and platform pitch (bottom row) for a 13 m/s simulation in DLC 1.2. Softwind  
555 (a, b), Hexafloat (c, d) and OC4 (e, f).

556 Various physical phenomena could cause such a difference in excitation. However, by process of exclusion, differences in  
557 hydrodynamic excitation are unlikely to be the cause of the increased self-excitation in QBlade, as nearly identical response  
558 in QBlade and OpenFAST was noted at the Softwind’s pitch natural frequency in part one of this study ((Behrens De Luna et  
559 al., 2023), Fig. 13). Moreover, the way unsteady aerodynamics are modelled is also not the cause, as switching to DBEM in  
560 QBlade did not improve agreement in this regard with respect to OpenFAST (not shown herein for brevity). In addition, as  
561 stated previously, OpenFAST does not include blade torsion. However, switching to a rigid structure did not improve the  
562 agreement of OpenFAST and QBlade. A possible explanation for the difference in blade pitch - platform pitch self-excitation  
563 was put forward in part one of this study (Behrens De Luna et al., 2023) and is related to increased aerodynamic torque  
564 variation in QBlade with respect to the other two codes. Indeed, upon further investigations, differences in the system  
565 dynamics, and how they interact with the control system, could explain the observed behavior. As explained in detail by Abbas  
566 et al. (Abbas et al., 2022), the controller and turbine can be seen as a closed-loop second-order system, characterized by a  
567 natural frequency at a certain operating wind speed:

$$\omega^2 = k_i(U_{op})B = k_i(U_{op}) \frac{N_g \partial \tau_a}{J \partial \beta} \quad (1)$$

569 where  $N_g$  and  $J$  are the gearbox ratio and rotor inertia, which are the same in OpenFAST, QBlade and DeepLines. The higher  
570 the natural frequency, the more responsive the system is to an external disturbance such as a platform pitch oscillation. The  
571 integral controller gain  $k_i$  is also the same in the two codes, as it depends on the controller tuning. The slope of the aerodynamic  
572 torque as a function of blade pitch is, however, different in the two codes. The derivative of aerodynamic torque as a function  
573 of blade pitch for the mean 11 m/s operating conditions is shown in Fig. 11 (b). As  $\frac{\partial \tau_a}{\partial \beta}$  is larger in magnitude for QBlade at  
574 the mean operating blade pitch of approximately  $0.5^\circ$ , from eq. 1,  $\omega^2$  is also larger, leading to increased self-excitation in

575 QBlade. This highlights how small differences in aerodynamics can lead to different controller response and influence turbine  
576 load predictions significantly.



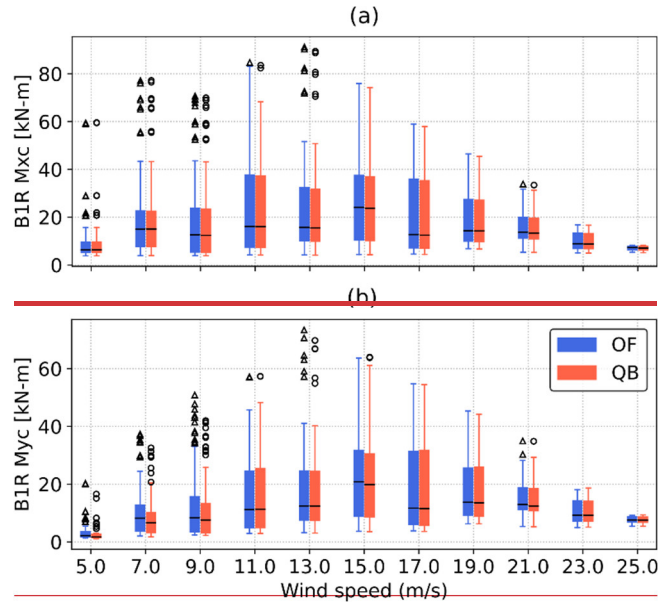
577  
578 **Figure 11: (a) aerodynamic torque as a function of blade pitch for OpenFAST and QBlade for 11 m/s operating TSR,**  
579 **and relative trendlines. (b) derivative of aerodynamic torque as a function of blade pitch computed from analytic**  
580 **derivative of trendlines.**

582 ~~These results can be put into perspective by comparing them to other authors' findings. Indeed, differences between BEM based~~  
583 ~~and LLFVW aerodynamic models in the prediction of blade root fatigue loads have also been noted by other authors. Boorsma~~  
584 ~~et al. (Boorsma et al., 2020) attributed the differences observed at 1P frequency to different induction tracking of the BEM~~  
585 ~~models during blade revolution, which causes differences in aerodynamic loading amplitude if wind shear, yaw misalignment,~~  
586 ~~rotor tilt and, in the case of FOWTs, platform pitch are present. In addition to 1P differences, Perez-Becker et al. (Perez-Becker~~  
587 ~~et al., 2020) also noted differences between LLFVW and BEM at low frequencies, the latter mainly being caused by different~~  
588 ~~blade pitch actuation in the models. In the context of FOWTs, Corniglion (Corniglion, 2022) also found blade root fatigue loads~~  
589 ~~predicted with a LLFVW model to be lower than those computed with a BEM-based aerodynamic tool. In this context, the higher~~  
590 ~~fatigue loads that are noted in OF are in line with these findings. The same cannot be said for DL however, that predicts lower~~  
591 ~~lifetime DELs than the LLFVW-based QB.~~

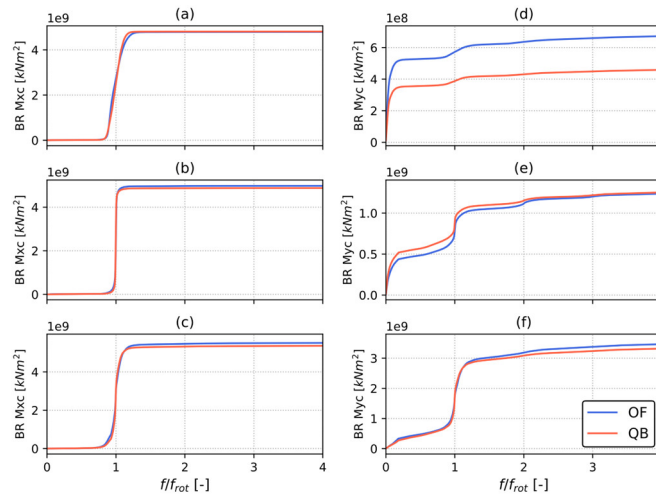
592 ~~As for the OC4 design, probability weighted 1Hz DELs are shown in Fig. 12. Better agreement between QB and OF is achieved~~  
593 ~~in this case, with the two codes being very close in 1Hz DEL prediction. The most relevant differences can be noted if BR Mye~~  
594 ~~1Hz DELs (Fig. 12 (b)) are compared at 5 m/s, 7 m/s and 9 m/s wind speed.~~

595 Despite QBlade and OpenFAST lifetime DELs being very close, the OC4 FOWT design highlights some interesting behavior,  
596 and differs in some key aspects from the Softwind FOWT design. CPSDs of blade root bending moments can, again, help  
597 investigate the causes of the differences in 1Hz-Lifetime DELs and are shown for the OC4 design in Figure 12. Focusing on  
598 out-of-plane root bending moment (TB My), Similarly to 1Hz DELs, differences in the CPSDs are very small. It is  
599 important to note that the differences in 1P excitation that are highlighted for the Softwind design (Fig. 10 Fig. 9) are not apparent

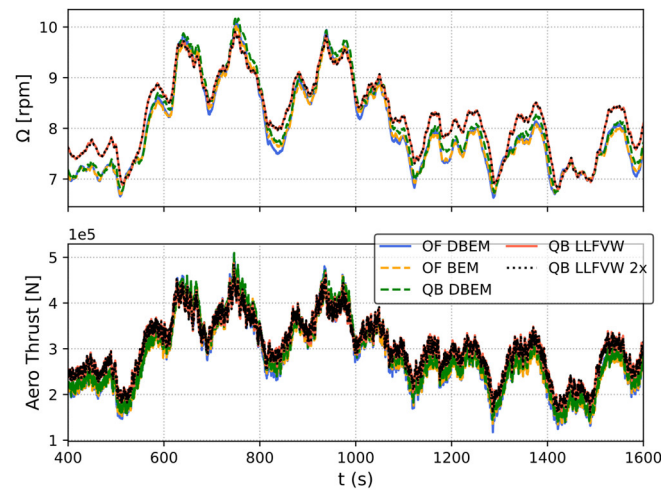
600 in OC4. In fact, some difference in this regard can only be noted at 7 m/s (Fig. 13 (d)). On the other hand, OF and QB are very  
 601 close at 13 m/s and 23 m/s (Fig. 13 (e, f)). The larger difference in 1P excitation between models on the Softwind design with  
 602 respect to the OC4 design can likely be explained by the size difference of the two rotors. As found by Madsen et al., (Madsen  
 603 et al., 2020) non-uniform rotor loading due to turbulence and wind shear increases with rotor size. For a larger rotor, a higher  
 604 portion of the eddies turbulent flow structures feature a length scale that is smaller than the rotor diameter, shifting a higher ratio  
 605 of the total energy in the turbulent spectrum from lower frequencies to the 1P frequency and multiples. As for wind shear, a  
 606 larger rotor operates in a larger portion of the atmospheric boundary layer, meaning that each blade experiences more inflow  
 607 variation during a revolution. As these phenomena increase in magnitude they are expected to increase the differences between  
 608 aerodynamic models at 1P frequency.



609 **Figure 12: Statistics of blade root bending moment in coned reference frame 1Hz zero mean Damage Equivalent Loads weighted by**  
 610 **the probability of each environmental bin they refer to for the OC4 test case. The boxes represent the 1<sup>st</sup> and 3<sup>rd</sup> quartiles, the whiskers**  
 611 **represent the data range and are found by adding/subtracting to the box edges 1.5 times the interquartile (IQR) range, the horizontal**  
 612 **line is the median of the data and flier values are shown as scatter points.**



614  
 615 **Figure 123:** Cumulative Power Spectral Density (CPSD) of blade root in-plane (a-c) and out-of-plane (d-f) bending moment for the  
 616 OC4 model. PSD is computed on all simulations with 7 m/s (a, d), 13 m/s (b, e) and 23 m/s (c, f) mean wind speed.  
 617



618  
 619 **Figure 143:** Time series of rotor speed and aerodynamic thrust in a 7 m/s simulation of the OC4 test-case. Various wake models are  
 620 compared; OpenFAST DBEM (Branlard et al., 2022), OpenFAST BEM (Ning et al., 2015), QBlade DBEM (Madsen et al., 2020) and  
 621 QBlade LLFVW (Marten, 2020).

622 On the other hand, the low frequency excitation difference that was noted for the Softwind design is also found for the OC4  
 623 design (Fig. 12 (d)) and. The main difference between OF and QB can be noted in Fig. 13 (d), where the CPSD of BR Myc in  
 624 OF is higher than QB at very low frequencies. A although not shown herein for brevity, this low frequency difference is also  
 625 found to be one of the main drivers the cause of the higher 1Hz-Lifetime DELs in OpenFAST in the 5 m/s and 9 m/s and wind  
 626 speed bins (Fig. 812). To better understand the causes of the higher DELs in OF in these wind speed bins, a difference that is

627 also noted for the SW model (Fig. 10 (a)) this difference, additional simulations were carried out with additional aerodynamic  
628 models in both QBlade and OpenFAST in an attempt to isolate the cause of such differences. Time series of rotor speed and  
629 aerodynamic thrust are shown in Fig. 14 for a 7 m/s mean wind speed simulation in DLC 1.2. This simulation was run with  
630 additional aerodynamic models in both QB and OF in an attempt to isolate the cause of such differences. In particular, OpenFAST  
631 simulations were performed using quasi-steady BEM without dynamic induction corrections (OpenFAST BEM). QBlade on the  
632 other hand was run using LLFVW with doubled wake length (LLFVW x2) and with the polar-BEM method (Madsen et al.,  
633 2020) (QBlade DBEM). Time series of rotor speed and aerodynamic thrust are shown in Fig. 13 for a 7 m/s mean wind speed  
634 simulation in DLC 1.2. As shown in Fig. 14 Fig. 13, larger variations in rotor speed can be noted in the BEM-based models. This  
635 phenomenon is present in both QBlade and OpenFAST and no improvement with respect to QBlade LLFVW is noted when a  
636 dynamic induction correction is used. On the other hand, doubling the wake length in the LLFVW simulation has little to no  
637 effect on rotor speed, indicating that the wake cut-off length used in the study is adequate. The larger rotor speed variation in  
638 BEM models causes rotor thrust to vary more as TSR varies, thus causing the additional low-frequency loading shown in Fig.  
639 14 Fig. 13.

640 These results can be put into perspective by comparing them to other authors' findings. Indeed, differences between BEM-based  
641 and LLFVW aerodynamic models in the prediction of blade root fatigue loads have also been noted by other authors. Boorsma  
642 et al. (Boorsma et al., 2020) attributed the differences observed at 1P frequency to different induction tracking of the BEM  
643 models during blade revolution, which causes differences in aerodynamic loading amplitude if wind shear, yaw misalignment,  
644 rotor tilt and, in the case of FOWTs, platform pitch are present. In addition to 1P differences, Perez-Becker et al. (Perez-Becker  
645 et al., 2020) also noted differences between LLFVW and BEM at low frequencies, the latter mainly being caused by different  
646 blade pitch actuation in the models. In the context of FOWTs, Corniglion (Corniglion, 2022) also found blade root fatigue loads  
647 predicted with a LLFVW model to be lower than those computed with a BEM-based aerodynamic tool. In this context, the higher  
648 fatigue loads that are noted in OpenFAST are in line with these findings. However, the same cannot be said for DeepLines  
649 however, that predicts lower lifetime DELs than the LLFVW-based QBlade.

#### 652 4.3.1 Tower Base and Mooring Fatigue Loads

653 Tower top, tower base and mooring lifetime DELs are shown in Fig. 15 Fig. 14 for the three FOWT designs. The lifetime DELs  
654 shown in Fig. 15 for the OC4 and Hexafloat designs show a similar trend to those shown in Fig. 8; lower lifetime DELs for  
655 DeepLines and higher Lifetime DELs for OpenFAST. Differently from blade root fatigue loads however, OpenFAST and  
656 DeepLines show good agreement in terms of lifetime DELs in Fig. 15 Fig. 14 for the Softwind design. Tower-related fatigue  
657 loads are lower than QBlade, while mooring line fatigue predictions are higher. In particular Moreover, differences in side-side  
658 tower loads (TT Fy and TB Mx) are in closer agreement, with differences being limited to 3% appear to be smaller than those  
659 found in the respective fore-aft sensors (TT Fx and TB My). These load sensors are arguably less influenced by aerodynamics

in these test cases, as the wind is always aligned with the global X direction, and more influenced by hydrodynamics. On the other hand as, wave headings range from -150° to 150° and thus influence side-side fatigue loads. In this context the good agreement in side-side loads is expected as hydrodynamics are modeled similarly in all three codes.

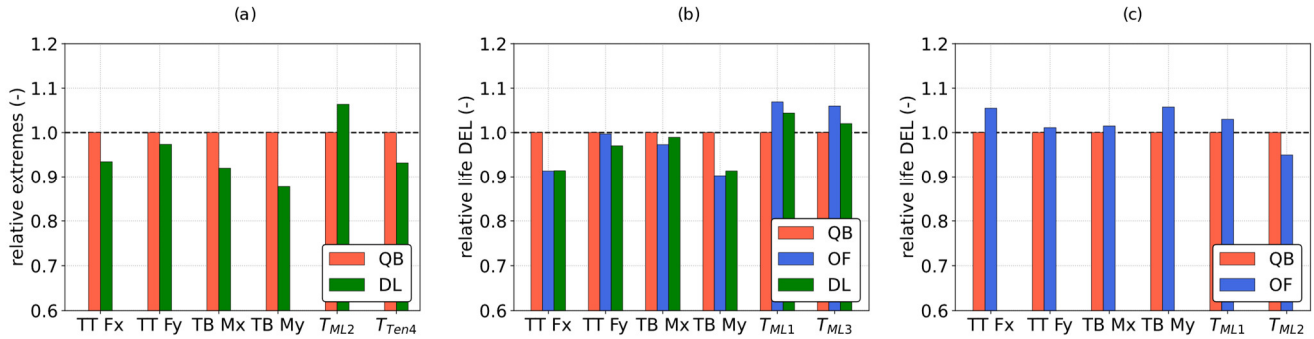


Figure 145: Lifetime DELs normalized with respect to values computed in QBlade. Yaw bearing shear forces in p coordinate system and tower base fore-aft and side-side bending moments and shear forces in t coordinate system. From left to right: DTU 10MW Hexafloat, DTU 10MW Softwind and NREL 5MW OC4.

The differences between the three models can be analyzed in more detail by comparing 1Hz DELs weighted by the probability of each environmental condition to occur:

$$\overline{DEL}_i = p_i * DEL = p_i \left( \frac{\sum_j n_j A_j^m}{t} \right)^{1/m} \quad (2)$$

$p_i$  is the probability of each condition to occur,  $n_j$  and  $A_j$  are the combinations of rainflow counted j-th number of cycles and amplitude in each simulation and m is the Wöhler curve exponent, equal to 10 for the composite blades and 4 for the other steel components. As discussed in Sect. 2.4, 1Hz DELs multiplied by their respective probability of occurrence are representative of the contribution to lifetime fatigue loads of each operating condition.

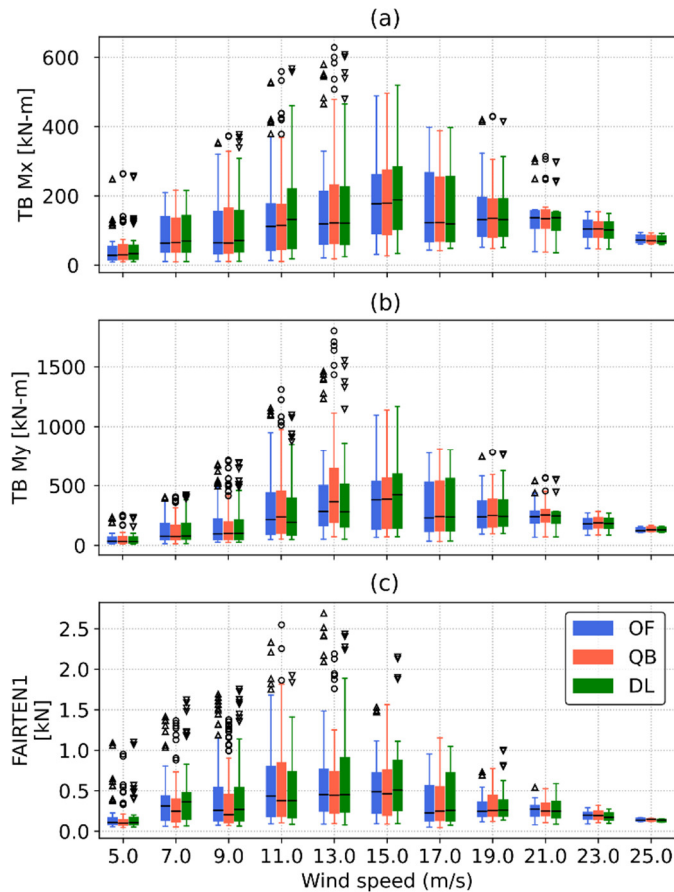
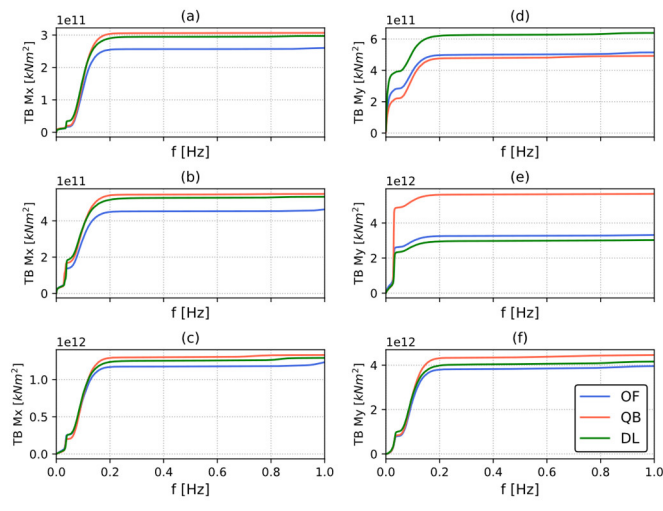


Figure 156: Statistics of tower base bending moment and fairlead tension 1Hz zero-mean Damage Equivalent Loads weighted by the probability of each environmental bin they refer to for the Softwind model. The boxes represent the 1<sup>st</sup> and 3<sup>rd</sup> quartiles, the whiskers represent the data range and are found by adding/subtracting to the box edges 1.5 times the interquartile (IQR) range, the horizontal line is the median of the data and flier values are shown as scatter points.

Statistics of tower base and fairlead tension of one of the upwind mooring lines 1Hz DELs for the Softwind design are shown in Fig. 16Fig. 15. Similarly to blade root bending moments, fromFrom a fatigue damage standpoint, the most relevant wind speeds are included between 9 m/s and 19 m/s wind speed. While 1Hz DELs are very close for all three numerical codes in Fig. 16Fig. 15 (a), the analysis of Fig. 16Fig. 15 (b) can help pinpoint the root cause of the increased Lifetime DEL prediction in QBlade. In fact, while the three codes agree well across most wind speeds, 1Hz DELs are statistically higher for QBlade particularly in the 11 m/s and 13 m/s wind speed bins. The CPSDs of tower base bending moments for the 7 m/s, 13 m/s and 23 m/s wind speed bins are shown in Figure 167. It stands out that tower base excitation is dominated by low-frequency peaks, corresponding to the floater's natural surge/sway and pitch/roll natural frequencies, and by response in the wave excitation frequency band. Moreover, contrary to blade root loads, 1P and 3P excitation is nearly irrelevant as the relative peaks located at approximately 0.3 Hz at 7 m/s and 0.5 Hz at 13 m/s and 23 m/s are one to two orders of magnitude smaller than the highest values of the respective PSDs. CPSDs show a flat profile from 0.2 Hz and upwards.



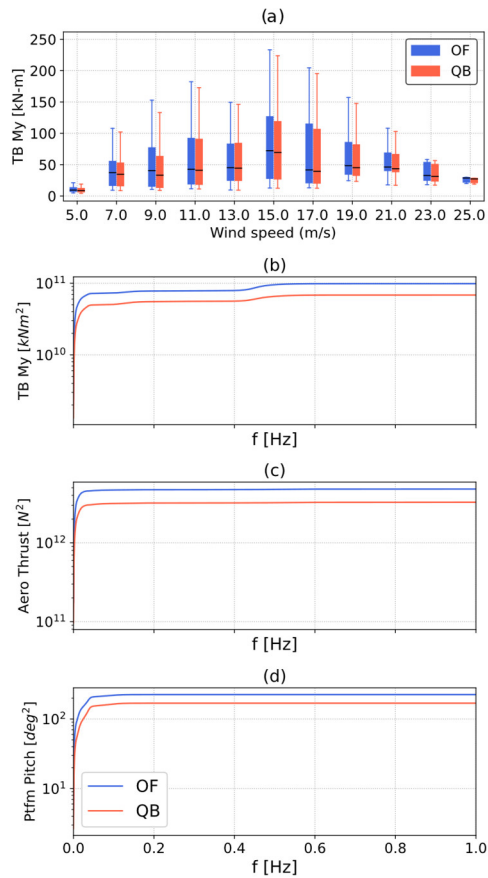


**Figure 176: Cumulative Power Spectral Density (CPSD) of tower base fore-aft side-side (a-c) and side-side fore-aft (d-f) bending moment for the Softwind test-case. CPSD is computed on all simulations with 7 m/s (a, d), 13 m/s (b, e) and 23 m/s (c, f) mean wind speed.**

Regarding fore-aft bending moment (TB My), at 7 m/s (Fig. 16 (d)), low-frequency aerodynamic excitation is the main driver of differences between QBlade – that shows lower response and fatigue loads at this wind speed – and the BEM-based codes. These differences are caused by the higher rotor speed variations recorded in OpenFAST and especially in DeepLines, as minimum rotor speed is not enforced in this code. The higher rotor speed variation leads to higher variation in aerodynamic forcing, as shown in Fig. 13. This phenomenon also contributes to the higher platform pitch variation that is observed for the BEM based codes (Fig. 4), further increasing low-frequency TB My excitation.

When analyzing Fig 16 (e), higher response at the floater pitch natural frequency is noted in QBlade. The cause of the increased response is floater-pitch blade-pitch instability, discussed in detail in Sect. 4.3.1

The same phenomenon also impacts the OC4 testcase, as shown in Fig. 17. The largest differences between OpenFAST and QBlade in the fore-aft tower base bending moment 1Hz DELs are located in the 9 m/s wind speed bin (Fig. 17 (a)). The CPSDs of aerodynamic thrust, platform pitch and TB My (Figs. 17 (b,c,d)) show that the main differences between the codes are found at very low frequencies, and are again caused by differences in aerodynamic response that are amplified by platform pitch and rotor speed variations.



709  
 710 **Figure 17: (a) Statistics of tower base fore-aft bending moment 1Hz zero-mean Damage Equivalent Loads weighted by the probability**  
 711 **of each environmental bin they refer to for the OC4 model. The boxes represent the 1<sup>st</sup> and 3<sup>rd</sup> quartiles, the whiskers represent the**  
 712 **data range and are found by adding/subtracting to the box edges 1.5 times the interquartile (IQR) range, the horizontal line is the**  
 713 **median of the data and flier values are shown as scatter points. (b,c,d) Cumulative Power Spectral Density (CPSD) of tower base fore-**  
 714 **aft bending moment, aerodynamic thrust and platform pitch for the OC4 design. PSD is computed on all simulations with 9 m/s mean**  
 715 **wind speed.**

716 Going back to the Softwind FOWT concept, at 13 m/s (Fig. 16 (e)) the largest difference between QBlade and the other codes  
 717 is at the floater pitch natural frequency, where TB My PSD is much larger in the former code. The higher response is caused by  
 718 the same phenomenon that causes higher blade root CPSDs at 13 m/s wind speed in QBlade (Fig. 9): floater and blade pitch self-  
 719 excitation. In the case of tower base loads, in addition to cyclic variation in aerodynamic loads, cyclic inertial and gravitational  
 720 forcing become relevant load sources, as the weight of the tower itself and the Rotor Nacelle Assembly (RNA) are considerable.  
 721 Therefore, despite QBlade comparing well to the other two codes at other wind speeds (Fig. 16 (f)), the difference highlighted  
 722 at 13 m/s (Fig. 16 (e)) ultimately leads to higher TB My lifetime DELs for QBlade (Fig. 14).

723 At 7 m/s (Fig. 17 (d)) the most relevant difference between the models is located at very low frequencies, where TB My peaks  
 724 and higher excitation can be seen in DL and OF. This low frequency excitation in the out of plane direction is related to  
 725 aerodynamic forcing, and the differences between the codes stem from the rotor speed difference that is discussed in Section

4.3.1 (Fig. 14). This difference does not significantly influence lifetime DELs (Fig. 15) as weighted TB My 1Hz DELs at this wind speed are small (Fig. 16). At 13 m/s the largest difference between QB and the other codes is at the floater pitch natural frequency, where TB My PSD is much larger in the former code. The higher PSD is caused by the same phenomenon that causes higher blade root 1Hz DELs at this wind speed in QB (Fig. 10): floater and blade pitch self-excitation. In the case of tower base loads, in addition to cyclic variation in aerodynamic loads, cyclic inertial and gravitational forcing become relevant load sources, as the weight of the tower itself and the Rotor Nacelle Assembly (RNA) are considerable. Therefore, despite QB comparing well to the other two codes at other wind speeds (Fig. 17 (d, f)), the difference highlighted at 13 m/s (Fig. 17 (e)) ultimately leads to higher TB My lifetime DELs for QB (Fig. 15).

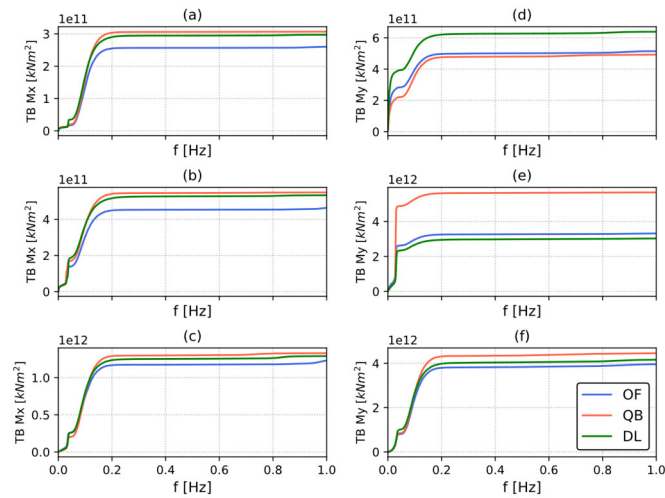


**Figure 17: Cumulative Power Spectral Density (CPSD) of tower base fore aft (a-c) and side side (d-f) bending moment for the SW test case. CPSD is computed on all simulations with 7 m/s (a, d), 13 m/s (b, e) and 23 m/s (c, f) mean wind speed.**

As shown in Fig. 18, finally, with respect to the floater and blade pitch self-excitation also influences fatigue load predictions for the Hexafloat model. As discussed previously, DeepLines predicts lower lifetime DELs than QBlade for this test case. The sensor where the difference is largest is TB My (Fig. 15). To investigate this further, weighted Contrary to floater-pitch-frequency frequency excitation 1Hz DELs statistics and PSDs for the 11 m/s and 13 m/s wind speed bins are shown in Figure 20. Weighted 1Hz DELs are also higher in QB in the 15 and 17 m/s wind speed bins, but the largest differences can be seen in the 11 m/s and 13 m/s bins. the peak in TB My response in correspondence of the tower first fore-aft natural frequency located at 0.2 Hz is captured well by both DeepLines and QBlade (Fig. 18 (b,c)). To investigate this further, the PSDs of TB My in these wind speed bins are shown in Fig. 20 (b) and (c). Thanks to its two body design, the HX platform allows for the use of a soft-stiff tower design. The first fore aft natural frequency is located at 0.2 Hz, and the peak in TB My response is captured well by both DL and QB (Fig. 20 (b,c)). While the two codes differ slightly throughout the frequency range in Fig. 20 (b), the largest

differences can be found below 0.02 Hz. The response peak located just below this frequency is the platform pitch natural frequency, and it is higher in QB in both Figs. 20 (a) and (c).

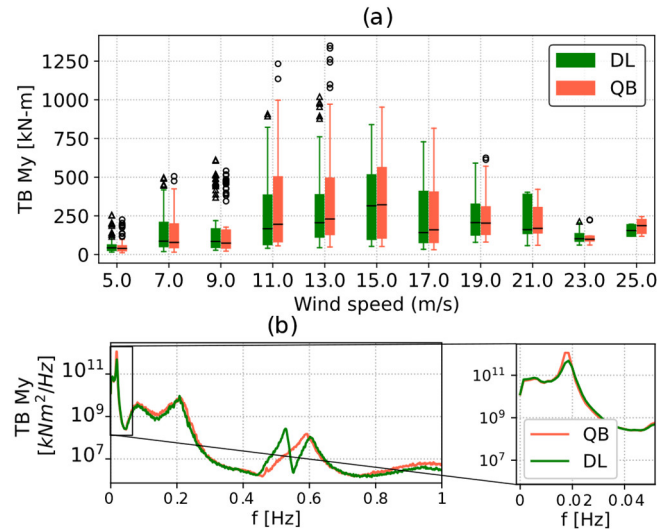


**Figure 18: (a) Statistics of fore-aft tower base bending moment 1Hz zero-mean Damage Equivalent Loads weighted by the probability of each environmental bin they refer to for the Hexafloat model. The boxes represent the 1<sup>st</sup> and 3<sup>rd</sup> quartiles, the whiskers represent the data range and are found by adding/subtracting to the box edges 1.5 times the interquartile (IOR) range, the horizontal line is the median of the data and flier values are shown as scatter points. (b) Power Spectral Density (PSD) of tower base fore-aft bending moment for the Hexafloat test-case. PSD is computed on all simulations with 11 m/s mean wind speed.**

Weighted tower base bending moment and fairlead tension DELs for the OC4 design are shown in Figure 18. The largest differences between OF and QB are in the fore-aft tower base bending moment and fairlead tension (Fig. 18 (b, c)) and are found in the 9 m/s and 15 m/s wind speed bins, where 1Hz DELs are higher for OF. The reason for such overestimation of TB My can be observed in Figure 19, where the PSD of TB My of simulations in the 9 m/s and 15 m/s wind speed bins are shown. The OC4 design features a soft-stiff tower design, and thus the natural frequency of the tower is located between the 1P and 3P frequencies. This can be seen clearly in Fig. 19 (b), where the peak in the PSD around 0.45 Hz is the tower natural frequency while 0.6 Hz is the 3P frequency. On the other hand, at 9 m/s the rotor speed is approximately 10 rpm (Fig. 3), and thus 3P frequency is approximately 0.5 Hz. Therefore, only one peak is visible in the PSD as 3P and fore-aft tower natural frequency are close. Some differences in TB My response can be noted in Fig. 19 (a) at this frequency, with OF being larger than QB. The main difference between the two codes is found at low frequencies, where response is higher for OF. This can be noted in the 15 m/s wind speed bin but even more so in the 9 m/s wind speed bin (Fig. 19 (a)), the latter being most likely connected to the increased rotor speed variation discussed in Fig. 14.

Finally, with respect to the HX model, as discussed previously, DL predicts lower lifetime DELs than QB. The sensor where the difference is largest is TB My (Fig. 15). To investigate this further, weighted 1Hz DELs statistics and PSDs for the 11 m/s and 13 m/s wind speed bins are shown in Figure 20. Weighted 1Hz DELs are also higher in QB in the 15 and 17 m/s wind speed

bins, but the largest differences can be seen in the 11 m/s and 13 m/s bins. To investigate this further, the PSDs of TB M<sub>y</sub> in these wind speed bins are shown in Fig. 20 (b) and (c). Thanks to its two-body design, the HX platform allows for the use of a soft-stiff tower design. The first fore-aft natural frequency is located at 0.2 Hz, and the peak in TB M<sub>y</sub> response is captured well by both DL and QB (Fig. 20 (b,c)). While the two codes differ slightly throughout the frequency range in Fig. 20 (b), the largest differences can be found below 0.02 Hz. The response peak located just below this frequency is the platform pitch natural frequency, and it is higher in QB in both Figs. 20 (a) and (c).

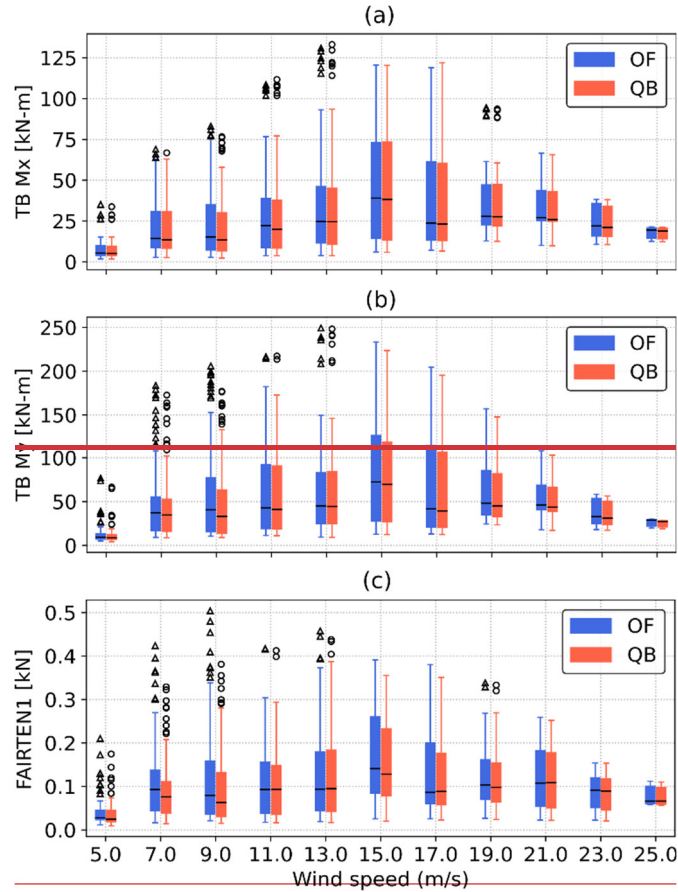
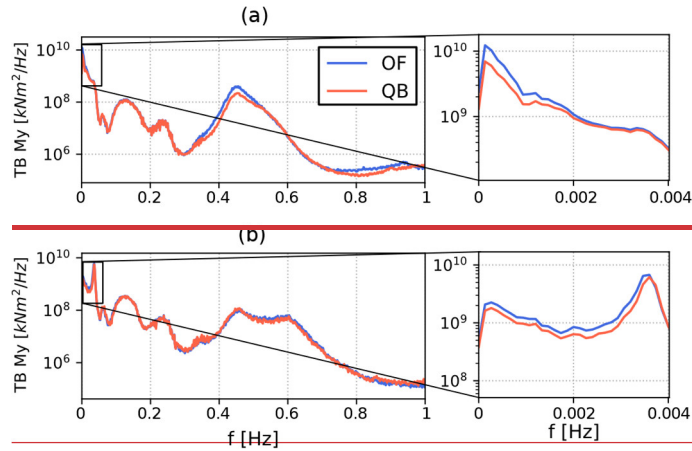
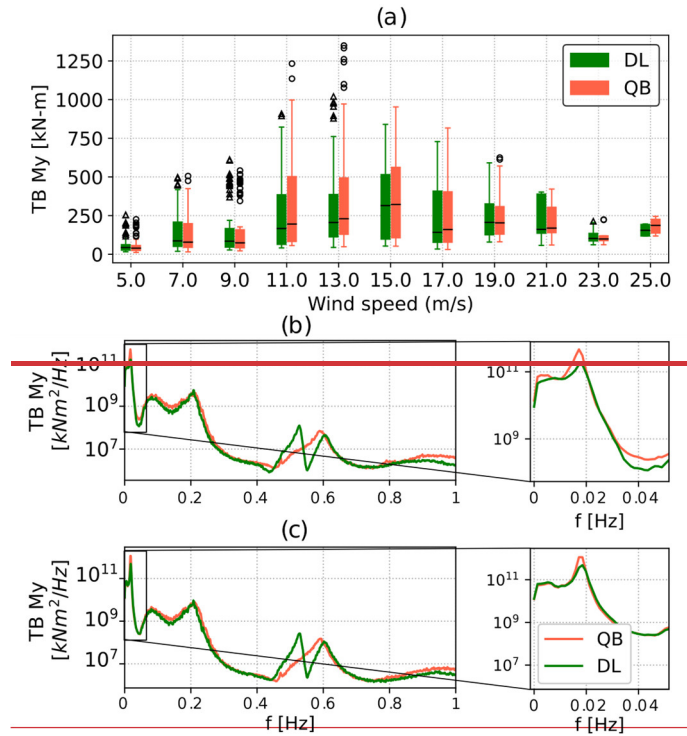


**Figure 18: Statistics of tower-base bending moment and fairlead tension 1Hz zero-mean Damage Equivalent Loads-weighted by the probability of each environmental bin they refer to for the OC4 model. The boxes represent the 1<sup>st</sup> and 3<sup>rd</sup> quartiles, the whiskers represent the data range and are found by adding/subtracting to the box edges 1.5 times the interquartile (IQR) range, the horizontal line is the median of the data and flier values are shown as scatter points.**



786  
787 **Figure 19: Power Spectral Density (PSD) of tower base fore-aft bending moment for the OC4 design. PSD is computed on all**  
788 **simulations with 9 m/s (a) and 15 m/s (b) mean wind speed.**



789  
790 **Figure 20: (a) Statistics of fore-aft tower base bending moment 1Hz zero-mean Damage Equivalent Loads weighted by the probability**  
791 **of each environmental bin they refer to for the HX model. The boxes represent the 1<sup>st</sup> and 3<sup>rd</sup> quartiles, the whiskers represent the**  
792 **data range and are found by adding/subtracting to the box edges 1.5 times the interquartile (IQR) range, the horizontal line is the**  
793 **median of the data and flier values are shown as scatter points. (b, c) Power Spectral Density (PSD) of tower base fore-aft bending**  
794 **moment for the OC4 test case. PSD is computed on all simulations with 11 m/s (b) and 13 m/s (c) mean wind speed.**

## 795 5 Conclusions

796 An extensive code-to-code comparison with realistic environmental conditions is performed in this study. Three floating wind  
797 turbine substructure designs, a semi-submersible, a spar-buoy and the Hexafloat concept proposed by Saipem are compared in  
798 multiple environmental conditions involving hundreds of simulations. The considered codes include TU Berlin's QBlade,  
799 NREL's OpenFAST and Principia's DeepLines. Statistics, extreme and fatigue loads of key load sensors are discussed.  
800 OpenFAST and QBlade results were refined over the span of several months, correcting small bugs that may arise in such a  
801 complex set-up and ultimately aligning the models better. DeepLines has not benefitted from such improvements due to budget  
802 and time limitations, which explains the poorer agreement noted for this code in many instances. These results are nevertheless  
803 included as they are representative of what could be achieved with limited time and budget often connected to industrial  
804 processes.

805 The statistical comparison revealed good agreement between the codes in their ability to predict general system dynamics.  
806 Nonetheless some differences, particularly in the coupling with the controller, emerged. Blade pitch – floater pitch self-excitation  
807 is noted in the Softwind and Hexafloat designs. While this phenomenon is present in all three codes, it is more accentuated in  
808 QBlade, despite all three sharing the blade pitch controller logic. A possible explanation for this phenomenon was put forward  
809 by the authors in a twin study (Behrens De Luna et al., 2023) and is linked to larger variations in rotor speed in QBlade. Above  
810 rated wind speed, such variations cause the pitch controller to intervene more aggressively, thus triggering the floater pitch  
811 instability. ~~Further research needs to be done to understand this phenomenon~~Upon further investigation, aerodynamic torque is  
812 found to be more sensitive to blade pitch variations at low wind speeds in QBlade, which causes the response of the coupled  
813 turbine and controller system to be faster and thus more prone to instability. This self-excitation is found to be the cause of  
814 increased fore-aft tower base and out-of-plane root bending moment lifetime DELs in QBlade in both the Hexafloat and Softwind  
815 designs and demonstrated how small differences in modeling can have a significant impact on design loads. No clear trend is  
816 noted when ultimate loads are compared. Taking QBlade as a reference point, ultimate loads are regularly found to be in the  
817  $\pm 15\%$  range, with only some exceeding it. The compared ultimate loads are selected according to the so-called “mean of max”  
818 method according to international standard indications (IEC61400-1, Annex G). As demonstrated in this work, small differences  
819 in ultimate loads may cause the method to select a different maximum, amplifying the difference between the models. In addition,  
820 the different FOWT designs have a different dynamical response to the environmental conditions, thus affecting the ultimate  
821 loads differently.

822 Fatigue loads, namely lifetime DELs, show a clear trend: OpenFAST generally predicts higher loads than QBlade, while  
823 DeepLines predicts lower lifetime fatigue loads. The reason for the latter being a different model set-up of the Softwind design  
824 in DeepLines and the lower effect of the blade pitch-platform pitch instability in the Hexafloat design. The exception to this is  
825 represented by tower base lifetime DELs, which for the Softwind design, are lower in OpenFAST. The root cause of this behavior  
826 in the Softwind design is again the floater pitch – blade pitch interaction, which is higher in QBlade compared to the two other  
827 codes. The higher DELs in OpenFAST are in line with other authors' findings, who observed higher fatigue loads in BEM-based



828 codes compared to in LLFVW-based codes. In this study however, OpenFAST differs from the other two codes also in the  
829 structural modeling: the former utilizing a modal structural model without the ability to model blade torsion while the latter two  
830 feature a multi-body model that includes blade torsion. Despite the trend being consistent between the codes, the magnitude of  
831 the lifetime DEL overestimation is different in the two designs where OpenFAST and QBlade are compared, OC4 and Softwind.  
832 In fact, in Softwind, blade root DELs are 2% to 14% higher in OpenFAST, while in OC4 they are up to 1.5% higher. The  
833 analysis of CPSDs highlighted greater response at the 1P frequency in OpenFAST in the latter design, while in OC4 the main  
834 difference between OpenFAST and QBlade is mostly confined to higher response in OpenFAST at very low frequencies. This  
835 low frequency difference is driven by increased rotor speed variation, in turn caused by differences in aerodynamic modeling.  
836 In conclusion, the relatively simpler model assumptions adopted in OpenFAST are found to be able to reproduce the system  
837 dynamics adequately for the considered designs. No clear trend is noted for extreme loads, with average differences of 15% that  
838 can be expected comparing the codes that depend on the specific design. In fact, differences between the codes are mostly in the  
839 +10% range, but deviations exceeding 20% were observed in some cases. Moreover, these differences could not be traced back  
840 to a specific engineering model or modelling choice. In this regard, including a larger set of extreme load cases with more  
841 parameter variations could help give a clearer picture of the differences in ultimate loading between the codes and the FOWT  
842 designs. On the other hand, a clear trend is noted in fatigue loads. This may be explained by the difference in aerodynamic  
843 models, in particular the comparison between the BEM-based OpenFAST and the LLFVW-based QBlade is consistent with  
844 existing scientific literature. DeepLines however contradicts this trend. While this may be, at least in part, due to setup differences  
845 in the Softwind design and to this code being less prone to blade pitch-floater pitch self-excitation, this aspect is identified as a  
846 key point for future research. Overall, the differences between the compared modelling theories are consistent with the existing  
847 body of literature on onshore wind turbines. The greater movement that FOWTs are allowed did not exacerbate the differences  
848 to the point that simpler models, such as OpenFAST, are outdated. This study has shown that, within the limitations highlighted  
849 in this and other similar works, these models are still relevant for industry and for many research applications.

850

## 851 **Nomenclature**

852	COD	Co-Directional
853	CPSD	Cumulative Power Spectral Density
854	CS	Coordinate System
855	DLC	Design Load Case
856	$E[\varepsilon_1   \varepsilon_2]$	Expected value of $\varepsilon_1$ conditioned on $\varepsilon_2$
857	ECD	Extreme Change of Direction with coherent gust
858	ESS	Extreme Sea State
859	ETM	Extreme Turbulence Model
860	EWM	Extreme Wind Model
861	FOWT	Floating Offshore Wind Turbine

862	MUL	Multi-Directional
863	NSS	Normal Sea State
864	NTM	Normal Turbulence Model
865	OC4	OC4\$ DeepCWind semi-submersible
866	<u>PSD</u>	<u>Power Spectral Density</u>
867	SSS	Severe Sea State
868	H <sub>s</sub>	Significant Wave Height (m)
869	T <sub>p</sub>	Peak Spectral Period (s)
870	M <sub>WW</sub>	Mean Wind-Wave misalignment (°)
871	U <sub>w</sub>	Wind Speed
872	V <sub>in</sub> /V <sub>out</sub>	Cut-in/Cut-out wind speed (m/s)
873		



**Funding** This work has received support from the FLOATECH project, funded by the European Union’s Horizon 2020 research and innovation programme under grant agreement No. 101007142

876

877 **Data Availability** The simulation results used in this study are publicly available at 10.5281/zenodo.7254241. The met-ocean  
878 conditions are also available at doi.org/10.1088/1742-6596/2385/1/012117. The QBlade-Ocean models upon which the models  
879 tested herein are based are available at 10.5281/zenodo.6397352 (OC5), 10.5281/zenodo.6397358 (Softwind),  
880 10.5281/zenodo.6397313 (Hexafloat) and the modifications required to align them with the models tested herein are detailed in  
881 10.5281/zenodo.7817707.

882

883 **Competing Interest** At least one of the (co-)authors is a member of the editorial board of Wind Energy Science. The peer-  
884 review process was guided by an independent editor, and the authors also have no other competing interests to declare.

## 885 **References**

886 Abbas, N. J., Zalkind, D. S., Pao, L., and Wright, A.: A reference open-source controller for fixed and floating offshore wind  
887 turbines, *Wind Energy Science*, 7, 53–73, <https://doi.org/10.5194/wes-7-53-2022>, 2022.

888 IEC TS 61400-3-2:2019 | IEC Webstore: <https://webstore.iec.ch/publication/29244>, last access: 3 January 2023.

889 Antonia Krieger, Gireesh K. V. Ramachandran, Luca Vita, Pablo Gómez Alonso, Gonzalo Gónzales Almeria, Joannès Barque,  
890 and Goren Aguirre: D7.2 LIFEs50+ Design Basis, 2015.

891 Arnal, V.: Experimental modelling of a floating wind turbine using a “software-in-the-loop” approach, These de doctorat,  
892 Ecole centrale de Nantes, 2020.

893 Bak, C., Zahle, F., Bitsche, R., Taeseong, K., Anders, Y., Henriksen, L. C., Natarajan, A., and Hansen, M. H.: Description of  
894 the DTU 10MW Reference Wind Turbine, DTU Wind Energy, Roskilde, Denmark, 2013.

- 895 Behrens De Luna, R., Perez-Becker, S., Saverin, J., Marten, D., Papi, F., Ducasse, M.-L., Bonnefoy, F., Bianchini, A., Nayeri,  
896 C. N., and Paschereit, C. O.: Verifying QBlade-Ocean: A Hydrodynamic Extension to the Wind Turbine Simulation Tool  
897 QBlade, *Wind Energy Science Discussions*, 1–36, <https://doi.org/10.5194/wes-2023-117>, 2023.
- 898 Bergua, R. and et. al.: OC6 Project Phase III: Validation of the Aerodynamic Loading on a Wind Turbine Rotor Undergoing  
899 Large Motion Caused by a Floating Support Structure, *Wind Energy Science Journal*, 8, 465–485, <https://doi.org/10.5194/wes-8-465-2023>, 2023.
- 901 Boorsma, K., Wenz, F., Lindenburg, K., Aman, M., and Kloosterman, M.: Validation and accommodation of vortex wake  
902 codes for wind turbine design load calculations, *Wind Energ. Sci.*, 5, 699–719, <https://doi.org/10.5194/wes-5-699-2020>, 2020.
- 903 Borg, M.: LIFES50+ Deliverable D1.2: Wind turbine models for the design, DTU Wind Energy, Risø, Denmark, 2015.
- 904 Branlard, E., Jonkman, B., Pirrung, G. R., Dixon, K., and Jonkman, J.: Dynamic inflow and unsteady aerodynamics models  
905 for modal and stability analyses in OpenFAST, *J. Phys.: Conf. Ser.*, 2265, 032044, <https://doi.org/10.1088/1742-6596/2265/3/032044>, 2022.
- 907 Buhl, M.: MExtremes User’s Guide, 9, 2015.
- 908 Burton, T. (Ed.): *Wind energy: handbook*, J. Wiley, Chichester ; New York, 617 pp., 2001.
- 909 Corniglion, R.: aero-elastic modeling of floating wind turbines with vortex methods, PhD Thesis, École des Ponts ParisTech,  
910 2022.
- 911 DNVGL: DNVGL-ST-0437 - Loads and site conditions for wind tubines, DNVGL AS, 2016.
- 912 DNVGL: DNVGL-ST-0119 - Floating wind turbine structures, DNVGL AS, 2018.
- 913 Faltinsen, O.: *Sea Loads on Ships and Offshore Structures*, Cambridge University Press, 1993.
- 914 Hansen, M. O. L.: *Aerodynamics of wind turbines*, 2nd ed., Earthscan, London ; Sterling, VA, 181 pp., 2008.
- 915 Haselsteiner, A. F., Lehmkuhl, J., Pape, T., Windmeier, K.-L., and Thoben, K.-D.: ViroCon: A software to compute  
916 multivariate extremes using the environmental contour method, *SoftwareX*, 9, 95–101,  
917 <https://doi.org/10.1016/j.softx.2019.01.003>, 2019.
- 918 Haselsteiner, A. F., Sander, A., Ohlendorf, J.-H., and Thoben, K.-D.: Global Hierarchical Models for Wind and Wave  
919 Contours: Physical Interpretations of the Dependence Functions, in: *Volume 2A: Structures, Safety, and Reliability*, ASME  
920 2020 39th International Conference on Ocean, Offshore and Arctic Engineering, Virtual, Online, V02AT02A047,  
921 <https://doi.org/10.1115/OMAE2020-18668>, 2020.
- 922 Haselsteiner, A. F., Coe, R. G., Manuel, L., Chai, W., Leira, B., Clarindo, G., Guedes Soares, C., Hannesdóttir, Á., Dimitrov,  
923 N., Sander, A., Ohlendorf, J.-H., Thoben, K.-D., Hauteclouque, G. de, Mackay, E., Jonathan, P., Qiao, C., Myers, A., Rode,  
924 A., Hildebrandt, A., Schmidt, B., Vanem, E., and Huseby, A. B.: A benchmarking exercise for environmental contours, *Ocean  
925 Engineering*, 236, 109504, <https://doi.org/10.1016/j.oceaneng.2021.109504>, 2021.
- 926 Hayman, G. J.: *MLife Theory Manual for Version 1.00*, NREL, 2012.
- 927 International Electrotechnical Commission: TS 61400-3-1, *Wind energy generation systems - Part 3-1: Design requirements  
928 for fixed offshore wind turbines*, 2019.

- 929 Jonkman, B. J.: TurbSim User's Guide v2.00.00, Renewable Energy, 2014.
- 930 Jonkman, J.: Definition of the Floating System for Phase IV of OC3, <https://doi.org/10.2172/979456>, 2010.
- 931 Jonkman, J. and Musial, W.: Offshore Code Comparison Collaboration (OC3) for IEA Task 23 Offshore Wind Technology  
932 and Deployment, Renewable Energy, 74, 2010.
- 933 Jonkman, J., Butterfield, S., Musial, W., and Scott, G.: Definition of a 5-MW Reference Wind Turbine for Offshore System  
934 Development, <https://doi.org/10.2172/947422>, 2009.
- 935 Jonkman, J. M. and Matha, D.: Dynamics of offshore floating wind turbines-analysis of three concepts, Wind Energ., 14, 557–  
936 569, <https://doi.org/10.1002/we.442>, 2011.
- 937 Kurnia, R., Ducrozet, G., and Gilloteaux, J.-C.: Second Order Difference- and Sum-Frequency Wave Loads in the Open-  
938 Source Potential Flow Solver NEMOH, ASME 2022 41st International Conference on Ocean, Offshore and Arctic  
939 Engineering, <https://doi.org/10.1115/OMAE2022-79163>, 2022.
- 940 Larsen, T. J. and Hanson, T. D.: A method to avoid negative damped low frequent tower vibrations for a floating, pitch  
941 controlled wind turbine, J. Phys.: Conf. Ser., 75, 012073, <https://doi.org/10.1088/1742-6596/75/1/012073>, 2007.
- 942 Le Cunff, C., Heurtier, J.-M., Piriou, L., Berhault, C., Perdrizet, T., Teixeira, D., Ferrer, G., and Gilloteaux, J.-C.: Fully  
943 Coupled Floating Wind Turbine Simulator Based on Nonlinear Finite Element Method: Part I — Methodology, in: Volume 8:  
944 Ocean Renewable Energy, ASME 2013 32nd International Conference on Ocean, Offshore and Arctic Engineering, Nantes,  
945 France, V008T09A050, <https://doi.org/10.1115/OMAE2013-10780>, 2013.
- 946 Lenfest, E., Goupee, A. J., Wright, A., and Abbas, N.: Tuning of Nacelle Feedback Gains for Floating Wind Turbine  
947 Controllers Using a Two-DOF Model, in: Volume 9: Ocean Renewable Energy, ASME 2020 39th International Conference  
948 on Ocean, Offshore and Arctic Engineering, Virtual, Online, V009T09A063, <https://doi.org/10.1115/OMAE2020-18770>,  
949 2020.
- 950 Madsen, H. A., Larsen, T. J., Pirrung, G. R., Li, A., and Zahle, F.: Implementation of the blade element momentum model on  
951 a polar grid and its aeroelastic load impact, Wind Energy Science, 5, 1–27, <https://doi.org/10.5194/wes-5-1-2020>, 2020.
- 952 Marten, D.: QBlade: a modern tool for the aeroelastic simulation of wind turbines, 2020.
- 953 Marten, D., Lennie, M., Pechlivanoglou, G., Nayeri, C. N., and Paschereit, C. O.: Implementation, optimization and validation  
954 of a nonlinear lifting line free vortex wake module within the wind turbine simulation code qblade, Proceedings of the ASME  
955 Turbo Expo, <https://doi.org/10.1115/GT2015-43265>, 2015.
- 956 Ning, A., Hayman, G., Damiani, R., and Jonkman, J. M.: Development and Validation of a New Blade Element Momentum  
957 Skewed-Wake Model within AeroDyn, in: 33rd Wind Energy Symposium, 33rd Wind Energy Symposium, Kissimmee,  
958 Florida, <https://doi.org/10.2514/6.2015-0215>, 2015.
- 959 Papi, F. and Bianchini, A.: Technical challenges in floating offshore wind turbine upscaling: A critical analysis based on the  
960 NREL 5 MW and IEA 15 MW Reference Turbines, Renewable and Sustainable Energy Reviews, 162, 112489,  
961 <https://doi.org/10.1016/j.rser.2022.112489>, 2022.
- 962 Papi, F. and Bianchini, A.: Annotated Guidelines for the Simulation of Floating Offshore Wind Turbines in a Real  
963 Environment, in: Proceedings of OMAE 2023, OMAE 2023, Melbourne, Australia, 2023.

- 964 Papi, F., Behrens De Luna, R., Saverin, J., Marten, D., Combreau, C., Troise, G., Mirra, G., and Bianchini, A.: D2.3. Design  
965 Load Case Database for Code-to-Code Comparison, 2022a.
- 966 Papi, F., Bianchini, A., Troise, G., Mirra, G., Marten, D., Saverin, J., Behrens De Luna, R., Ducasse, M.-L., and Honnet, J.:  
967 D2.4. Full report on the estimated reduction of uncertainty in comparison to the state-of-the-art codes OpenFAST and  
968 DeepLines Wind™, FLOATECH, 2022b.
- 969 Papi, F., Perignon, Y., and Bianchini, A.: Derivation of Met-Ocean Conditions for the Simulation of Floating Wind Turbines:  
970 a European case study, *J. Phys.: Conf. Ser.*, 2385, 012117, <https://doi.org/10.1088/1742-6596/2385/1/012117>, 2022c.
- 971 Papi, F., Bianchini, A., Troise, G., Mirra, G., Marten, D., Saverin, J., Behrens de Luna, R., Ducasse, M.-L., and Honnet, J.:  
972 Deliverable 2.4 Full report on the estimated reduction of uncertainty in comparison to the state-of-the-art codes OpenFAST  
973 and DeepLines Wind, 2023.
- 974 Perez-Becker, S., Papi, F., Saverin, J., Marten, D., Bianchini, A., and Paschereit, C. O.: Is the Blade Element Momentum  
975 theory overestimating wind turbine loads? – An aeroelastic comparison between OpenFAST’s AeroDyn and QBlade’s Lifting-  
976 Line Free Vortex Wake method, *Wind Energ. Sci.*, 5, 721–743, <https://doi.org/10.5194/wes-5-721-2020>, 2020.
- 977 Perez-Becker, S., Saverin, J., Behrens de Luna, R., Papi, F., Combreau, C., Ducasse, M.-L., Marten, D., and Bianchini, A.:  
978 Deliverable 2.2 - Validation Report of QBlade-Ocean, 2022.
- 979 Robertson, A. and Jonkman, J.: Loads Analysis of Several Offshore Floating Wind Turbine Concepts, International Society of  
980 Offshore and Polar Engineers 2011 Conference, Maui, Hawaii, 10, 2011.
- 981 Robertson, A., Jonkman, J., Masciola, M., Song, H., Goupee, A., Coulling, A., and Luan, C.: Definition of the Semisubmersible  
982 Floating System for Phase II of OC4, <https://doi.org/10.2172/1155123>, 2014a.
- 983 Robertson, A., Jonkman, J., Vorpahl, F., Popko, W., Qvist, J., Frøyd, L., Chen, X., Azcona, J., Uzunoglu, E., Guedes Soares,  
984 C., Luan, C., Yutong, H., Pengcheng, F., Yde, A., Larsen, T., Nichols, J., Buils, R., Lei, L., Nygaard, T. A., Manolas, D.,  
985 Heege, A., Vatne, S. R., Ormberg, H., Duarte, T., Godreau, C., Hansen, H. F., Nielsen, A. W., Riber, H., Le Cunff, C., Beyer,  
986 F., Yamaguchi, A., Jung, K. J., Shin, H., Shi, W., Park, H., Alves, M., and Guérinel, M.: Offshore Code Comparison  
987 Collaboration Continuation Within IEA Wind Task 30: Phase II Results Regarding a Floating Semisubmersible Wind System,  
988 in: Volume 9B: Ocean Renewable Energy, ASME 2014 33rd International Conference on Ocean, Offshore and Arctic  
989 Engineering, San Francisco, California, USA, V09BT09A012, <https://doi.org/10.1115/OMAE2014-24040>, 2014b.
- 990 Robertson, A. N., Wendt, F., Jonkman, J. M., Popko, W., Dagher, H., Gueydon, S., Qvist, J., Vittori, F., Azcona, J., Uzunoglu,  
991 E., Soares, C. G., Harries, R., Yde, A., Galinos, C., Hermans, K., de Vaal, J. B., Bozonnet, P., Bouy, L., Bayati, I., Bergua, R.,  
992 Galvan, J., Mendikoa, I., Sanchez, C. B., Shin, H., Oh, S., Molins, C., and Debruyne, Y.: OC5 Project Phase II: Validation of  
993 Global Loads of the DeepCwind Floating Semisubmersible Wind Turbine, *Energy Procedia*, 137, 38–57,  
994 <https://doi.org/10.1016/j.egypro.2017.10.333>, 2017.
- 995 Robertson, A. N., Gueydon, S., Bachynski, E., Wang, L., Jonkman, J., Alarcón, D., Amet, E., Beardsell, A., Bonnet, P., Boudet,  
996 B., Brun, C., Chen, Z., Féron, M., Forbush, D., Galinos, C., Galvan, J., Gilbert, P., Gómez, J., Harnois, V., Haudin, F., Hu, Z.,  
997 Dreff, J. L., Leimeister, M., Lemmer, F., Li, H., Mckinnon, G., Mendikoa, I., Moghtadaei, A., Netzband, S., Oh, S., Pegalajar-  
998 Jurado, A., Nguyen, M. Q., Ruehl, K., Schünemann, P., Shi, W., Shin, H., Si, Y., Surmont, F., Trubat, P., Qvist, J., and  
999 Wohlfahrt-Laymann, S.: OC6 Phase I: Investigating the underprediction of low-frequency hydrodynamic loads and responses  
1000 of a floating wind turbine, *J. Phys.: Conf. Ser.*, 1618, 032033, <https://doi.org/10.1088/1742-6596/1618/3/032033>, 2020.
- 1001 Stewart, G. M.: Design Load Analysis of Two Floating Offshore Wind Turbine Concepts, University of Massachusetts  
1002 Amherst, <https://doi.org/10.7275/7627466.0>, 2016.

1003 Valamanesh, V., Myers, A. T., and Arwade, S. R.: Multivariate analysis of extreme metocean conditions for offshore wind  
1004 turbines, *Structural Safety*, 55, 60–69, <https://doi.org/10.1016/j.strusafe.2015.03.002>, 2015.

1005 Van Garrel, A.: Development of a wind turbine aerodynamics simulation module, 2003.

1006 Vigarra, F., Cerdán, L., Durán, R., Muñoz, S., Lynch, M., Doole, S., Molins, C., Trubat, P., and Gunache, R.: COREWIND  
1007 D1.2 Design Basis, , <https://doi.org/10.5281/zenodo.4518828>, 2020.

1008 Wang, L., Robertson, A., Jonkman, J., and Yu, Y.-H.: OC6 phase I: Improvements to the OpenFAST predictions of nonlinear,  
1009 low-frequency responses of a floating offshore wind turbine platform, *Renewable Energy*, 187,  
1010 <https://doi.org/10.1016/j.renene.2022.01.053>, 2022.

1011 Yu, W.: D4.2 Public Definition of the Two LIFES50+ 10MW Floater Concepts, 32, n.d.

1012

1013

1014

1015

1016

1017

1018

1019

1020

1021

1022

1023

1024

1025

1026

1027

1028

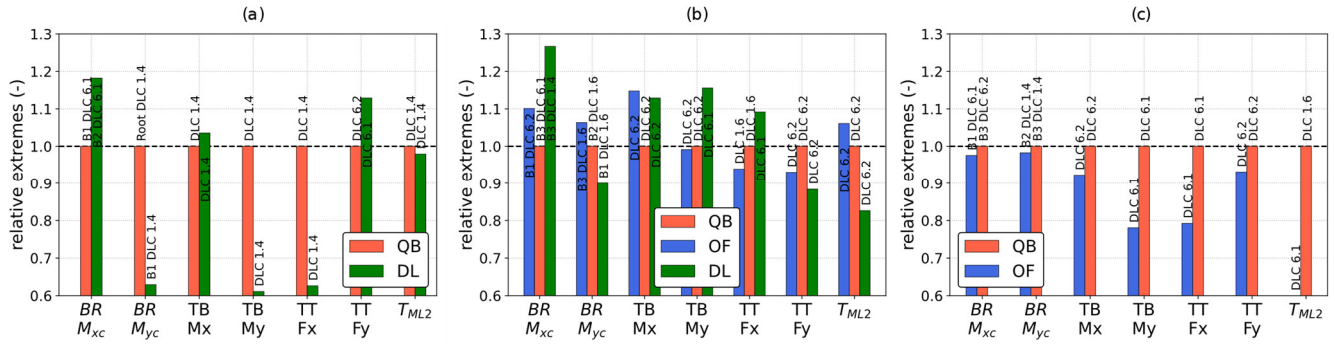
1029

1030

1031

### 1032 6 Appendix A – Minimum Ultimate Loads

1033



1034

1035 **Figure A1: Selection of ultimate loads (minimum) recorded in the three simulation codes. (a) DTU 10MW Hexafloat, (b) DTU 10MW**  
1036 **Softwind and (c) NREL 5MW OC4.**

1037